Bioactive Materials 27 (2023) 216–230

Contents lists available at ScienceDirect

Bioactive Materials

journal homepage: www.keaipublishing.com/en/journals/bioactive-materials

3D-printed scaffolds with 2D hetero-nanostructures and immunomodulatory cytokines provide pro-healing microenvironment for enhanced bone regeneration

Xifeng Liu [a,b], Bipin Gaihre [a,b], Sungjo Park [c], Linli Li [a,b], Babak Dashtdar [a,b], Maria D. Astudillo Potes [a,b], Andre Terzic [c], Benjamin D. Elder [a,b,d], Lichun Lu [a,b,*]

[a] Department of Physiology and Biomedical Engineering, Mayo Clinic, Rochester, MN, 55905, USA
[b] Department of Orthopedic Surgery, Mayo Clinic, Rochester, MN, 55905, USA
[c] Department of Cardiovascular Medicine and Center for Regenerative Medicine, Mayo Clinic, Rochester, MN, 55905, USA
[d] Department of Neurologic Surgery, Mayo Clinic, Rochester, MN, 55905, USA

ARTICLE INFO

Keywords:
3D-printing
2D materials
Bone repair
Osteo-immunomodulation
Cytokines

ABSTRACT

Three-dimensional (3D) printing technology is driving forward the progresses of various engineering fields, including tissue engineering. However, the pristine 3D-printed scaffolds usually lack robust functions in stimulating desired activity for varied regeneration applications. In this study, we combined the two-dimensional (2D) hetero-nanostructures and immuno-regulative interleukin-4 (IL-4) cytokines for the functionalization of 3D-printed scaffolds to achieve a pro-healing immuno-microenvironment for optimized bone injury repair. The 2D hetero-nanostructure consists of graphene oxide (GO) layers, for improved cell adhesion, and black phosphorous (BP) nanosheets, for the continuous release of phosphate ions to stimulate cell growth and osteogenesis. In addition, the 2D hetero-nanolayers facilitated the adsorption of large content of immuno-regulative IL-4 cytokines, which modulated the polarization of macrophages into M2 phenotype. After *in vivo* implantation in rat, the immuno-functioned 3D-scaffolds achieved *in vivo* osteo-immunomodulation by building a pro-healing immunological microenvironment for better angiogenesis and osteogenesis in the defect area and thus facilitated bone regeneration. These results demonstrated that the immuno-functionalization of 3D-scaffolds with 2D hetero-nanostructures with secondary loading of immuno-regulative cytokines is an encouraging strategy for improving bone regeneration.

1. Introduction

Three-dimensional (3D) printing technology is driving forward the progress of various engineering fields, including manufacturing engineering, materials engineering, biomedical engineering, and tissue engineering [1–4]. In the regenerative medicine and tissue engineering field, 3D-printing technique was applied to achieve spatial geometric configuration with preferred internal structure design for a large variety of metal, inorganic, ceramics, and polymeric biomaterials [5,6]. With gradual advances in technology, the current 3D printing is able to manufacture sophisticated architectures that can provide mechanical and biochemical support for tissue infiltration, integration, and restoration function. With these advantages, 3D-printing technology has been applied in various biomedical applications, e.g., fracture healing, segmental bone defect repair, oral repair, skin injury repair, cardiovascular diseases, and spinal fusion [7–10].

For bone injury repair, 3D printing was used to fabricate scaffolds with interconnected pores fitting bone shape and injury defect morphology [11–13]. The porous structure allows space for the immediate infiltration of cells and tissues into the scaffolds, promoting better tissue-implant integration [11–13]. The porosity also reduces material mass allowing faster degradation of the scaffolds and expanding the bio-interface area for cell attachment and growth. In the past decades, researchers have tried intensively to develop implants using 3D printing of various materials, including titanium metals, bioglasses, ceramics, and non-biodegradable or biodegradable polymers [9,14,15].

Peer review under responsibility of KeAi Communications Co., Ltd.
* Corresponding author. Department of Physiology and Biomedical Engineering, Mayo Clinic, Rochester, MN, 55905, USA.
E-mail address: Lu.Lichun@mayo.edu (L. Lu).

https://doi.org/10.1016/j.bioactmat.2023.03.021
Received 12 December 2022; Received in revised form 23 March 2023; Accepted 24 March 2023
2452-199X/© 2023 The Authors. Publishing services by Elsevier B.V. on behalf of KeAi Communications Co. Ltd. This is an open access article under the CC BY-NC-ND license (http://creativecommons.org/licenses/by-nc-nd/4.0/).

Biodegradable polymers that can be adsorbed *in situ* without additional surgery after implantation, e.g., poly(L-lactic acid) (PLLA) [16], poly (lactic-co-glycolic acid) (PLGA) [17], poly(ε-caprolactone) (PCL) [18], and poly(propylene fumarate) (PPF) [19,20], are among the primary research focus for bone repair. In our previous work, we have constructed a series of 3D-printed PPF stents and tested to have outstanding *in vitro* osteogenic induction and *in vivo* bone repair after implantation [21,22].

However, these pristine 3D-printed scaffolds usually do not possess robust functions to stimulate desired cellular activities for varied regeneration applications. For example, in bone injury repair, the implants are expected to have a strong attraction of stem cells to the material surface, followed by timely induction of neovascularization and osteogenesis in the injury site to assist bone healing. In addition, suitable immuno-regulation of the injury site into a regeneration-friendly microenvironmental niche is also critical to prevent bone non-union at early-stage and expedite later-on bone regeneration. Nonetheless, pure 3D-printed scaffolds require further functionalization in order to meet these various requirements.

One of the most important solutions to solve this deficiency is to surface coat a layer of material that, by nature, has the required properties for the 3D-scaffolds. In this manner, the 3D-scaffolds can gain the desired functions without altering their original properties, e.g., geometric configuration, mechanical strength, and biodegradation rates. In our previous studies, we functionalized the 3D-printed scaffolds with two-dimensional (2D) materials and achieved improved protein adsorption, cell attraction, and osteogenesis [23,24]. Phosphorene nanosheet (PNS), also named black phosphorus (BP) nanosheet, is a 2D material with extraordinary potential for regenerative medicine, taking advantage of its excellent biocompatibility and continuous phosphate ion release during the oxidation process [25,26]. Phosphate is the basic component that builds the phosphate backbone for DNA & RNA, and the phospholipid bilayer in the cell membrane; thus is indispensable for cell signaling, proliferation, and differentiation [27–29]. Sufficient supply of phosphate ions is critical for skeleton development, as well as cell growth and osteogenesis during bone injury repair [30,31]. Graphene oxide (GO) nanosheet is a 2D nanomaterial that has been widely reported to elevate cell adhesion, proliferation, and differentiation [32–34]. 3D-scaffolds incorporated with GO were observed to support stem cell differentiation, angiogenesis, and osteogenesis [35,36].

In addition to phosphate supply and osteogenesis, most recent studies found that the immune microenvironment at the bone injury site is important for bone tissue regeneration [37–39]. In responding to varied environmental signals, macrophages have the potential to polarize into pro-inflammatory M1 phenotype, which stimulates inflammation and fibrosis, or into pro-healing M2 phenotype, which assists stem cell osteogenesis and extracellular matrix (ECM) remodeling for bone repair [40]. The previous report has observed that adequate polarization of macrophages into M2 phenotype may create an osteoimmune friendly microenvironment by stimulating the secretion of pro-osteogenic growth factors, e.g., bone morphogenetic protein-2 (BMP-2) and vascular endothelial growth factor (VEGF) [41]. In consideration of that, various techniques were explored to achieve an osteoimmune friendly microenvironment for bone implants, including optimization of topography [42], adjustment of surface hydrophilicity [43,44], doping with immuno-regulative Ca^{2+}, Cu^{2+}, Zn^{2+}, Sr^{2+} metal ions [45–48], or surficial delivery of immuno-modulative cytokines such as interleukin-4 (IL-4) [49].

In this study, we combined the 2D nanomaterials and immuno-regulative cytokines for the functionalization of 3D-printed scaffolds to achieve a pro-healing immuno-microenvironment for optimized bone injury repair (Fig. 1a). The 3D-scaffolds were printed with a polymeric

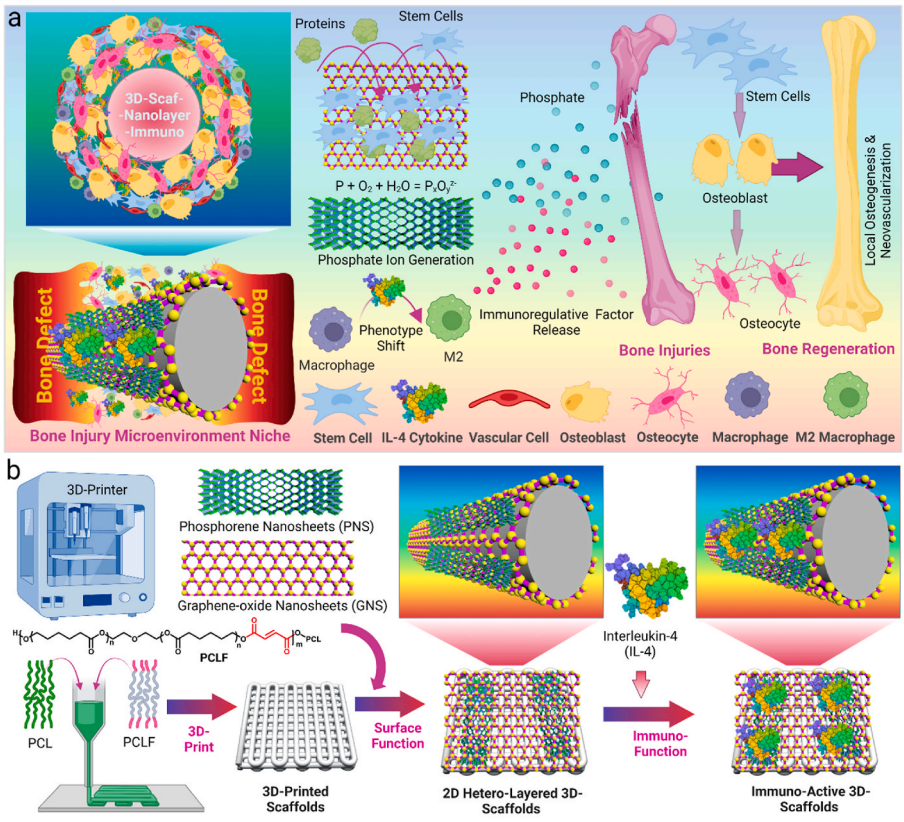

Fig. 1. a). Schematic demonstration of osteo-immunomodulation directed bone repair using 3D scaffolds functionalized with 2D hetero-nanostructures and cytokines. b) The process of creating immuno-active 3D printed scaffolds using a thermoplastic extrusion 3D printer followed by surficial coating of 2D materials and loading with cytokines.

ink, and surface coated with 2D GO nanosheets, or BP nanosheets, or GOBP hetero-nanostructures (Fig. 1b). GO layers were applied to improve cell adhesion to the 3D-scaffolds, and BP nanosheets were used to generate continuous phosphate release to stimulate cell growth and osteogenesis. In addition, these 2D materials help to adsorb significant amounts of IL-4 cytokines to the 3D-scaffolds surface, which modulates the polarization of macrophages into M2 phenotype and builds a pro-healing microenvironment for better angiogenesis and osteogenesis. The *in vitro* biocompatibility, stem cell adhesion, proliferation, and osteogenesis of the functionalized 3D-scaffolds were characterized. After immuno-function with IL-4 cytokine, the macrophage phenotypic polarization was also determined. Following implantation in a rat calvarial defect model, the *in vivo* bone regeneration, bone volume to tissue volume (BV/TV) ratio, bone mineral density (BMD), and new bone area, were evaluated using micro-CT scanning. The *in vivo* osteogenesis, neovascularization, and *in vivo* macrophage M2 phenotype polarization in the bone defect site with implanted 3D-scaffolds were also studied. Overall, this study reports a facile and versatile route for the functionalization of 3D-printed implants with osteoinductive 2D materials and immuno-regulative cytokines to create favorable pro-healing microniche for enhanced *in vivo* bone regeneration.

2. Materials and methods

2.1. Synthesis of 2D materials and polymers

GO nanolayers were produced from natural graphite (Sigma Aldrich, Milwaukee, WI) after oxidation and exfoliation using an improved Hummers' method [50,51]. Phosphorene nanolayers were obtained from black phosphorous powder (ACS Material LLC, Pasadena, CA) by liquid exfoliation [52,53]. Poly(caprolactone fumarate) (PCLF), a crosslinkable polymer for 3D printing, was synthesized using polycaprolactone diol (M_n ~2000) according to previous reports [54].

2.2. 3D-printing of scaffolds

PCLF polymer (7 g) and polycaprolactone (average M_n 80,000, 3 g) were dissolved in 20 mL dichloromethane with constant stirring. After dissolving, the solution was added with 0.5 wt% of photo-initiator bisacrylphosphrine oxide (BAPO, Ciba Specialty Chemicals, Tarrytown, NY), then air-dried under protection from light in a large area container. Scaffolds with dimensions around 30 mm × 30 mm × 1 mm (width × length × height) were printed using a BIO X 3D Bioprinter (CELLINK, Boston, MA). After printing, scaffolds were cured under 365 nm UV light for 2 h, then ammonolyzed in 100 mL isopropyl alcohol ammonolysis solution containing 6.0 g of hexamethylenediamine (Sigma Aldrich) for 10–20 min at 37 °C. The obtained 3D-scaffolds were washed in excessive de-ionized (DI) water for 2–4 days to remove excess photoinitiator and residues, then air-dried to obtain 3D-scaffolds.

2.3. Functionalization of 3D-scaffolds with 2D hetero-nanostructures

The 3D-printed scaffolds were punched into round disks using a biopsy punch (diameter 4.5 mm), then immersed in BP solution (1 mg/mL), GO solution (1 mg/mL), or GOBP solution (1 mg/mL BP and 1 mg/mL GO), respectively. After 1 h, the samples were taken out, and dried under vacuum to obtain 3D-Scaf-BP, 3D-Scaf-GO, and 3D-Scaf-GOBP scaffolds, respectively.

2.4. Material characterizations

Scanning electron microscopy (SEM). After sputter coating with gold-palladium, phosphorous nanosheets, GO nanosheets, GOBP hetero-nanostructures, and 3D-scaffolds were imaged on a Scanning electron microscope (S-4700, Hitachi Instruments, Tokyo, Japan).

Transmission electron microscopy (TEM). The morphology of phosphorous nanosheets and GO nanosheets was imaged using a transmission electron microscope (1200-EX II, JEOL Inc., Japan).

Atomic force microscopy (AFM). The obtained GO and BP nanosheets were tested on a Nanoscope IV PicoForce Multimode AFM (Bruker, Santa Barbara, CA) to determine the morphology and height of the nanosheets [55].

Protein adsorption on 3D-printed scaffolds. The 3D scaffolds were immersed in a cell culture medium containing Dulbecco's modified Eagle's medium (DMEM, Gibco) supplemented with 10% fetal bovine serum (FBS, Gibco) for 2 h at 37 °C. After being rinsed 3 times with phosphate-buffered saline (PBS), the total proteins on the 3D-scaffolds were washed off using 1% sodium dodecyl sulfate (SDS, Bio-Rad Laboratories, Hercules, CA) and tested by a microBCA protein assay kit (Pierce, Rockford, IL).

Phosphate release from 3D-scaffolds. The 3D-scaffolds were immersed in 1 mL of DI H_2O in a vial. At designated time points, 0.4 mL of released solution was taken out, and the phosphate concentration was tested using a phosphate assay kit (ab65622, Abcam, Cambridge, UK). The vial was refilled with the same amount of fresh DI H_2O.

2.5. Cytotoxicity of functioned 3D-scaffolds

Live/dead staining. The 3D-scaffolds were sterilized under UV irradiation for 2 h in a tissue culture hood and then attached to the bottom of wells of 48-well tissue culture polystyrene (TCPS) plates using high vacuum grease (Dow Corning, Midland, MI). After seeding with rat bone marrow mesenchymal stem cells (rBMSCs, Fisher Scientific), the scaffolds were cultured in low glucose DMEM supplemented with fetal bovine serum (FBS, 10%, Gibco) and penicillin−streptomycin (Pen-Strep, 0.5%, Gibco) for 3 days, then stained with a LIVE/DEAD® Cell Imaging Kit (Thermo Fisher Scientific) and imaged on an inverted laser scanning confocal microscope (Carl Zeiss, Germany).

Cytotoxicity of 3D-scaffolds leaching medium. The sterilized 3D-scaffolds were placed in transwells (mesh size 3 μm) and co-cultured with rBMSCs for 3 and 7 days. The medium was then replaced by MTS solution (CellTiter 96, Promega, Madison, WI), and the optical density value at 490 nm was read by UV–vis absorbance microplate reader (SpectraMax Plus 384, Molecular Devices, Sunnyvale, CA).

2.6. Stem cell proliferation and osteogenesis

The rBMSCs were seeded on sterilized 3D-scaffolds and cultured for 1, 3, and 7 days. The proliferated cell numbers on each scaffold were tested by the MTS assay, and the absorbance at 490 nm was read using the UV–vis absorbance microplate reader. For immuno-fluorescence staining, rBMSCs on the 3D-scaffolds were fixed using paraformaldehyde (PFA, 4% solution) and permeabilized with 0.2% Triton X-100. Cells were then stained with *anti*-vinculin−FITC antibody (1:50 dilution; Sigma-Aldrich) and rhodamine-phalloidin (1:200 dilution; Cytoskeleton Inc, Denver, CO, USA) at 37 °C for 1 h. After staining with 4′,6-diamidino-2-phenylindole (DAPI) for 2 min, the immune-fluorescence labeled cells on the functionalized 3D-scaffolds were imaged using an inverted laser scanning confocal microscope (Carl Zeiss).

To determine the osteogenic potential, the rBMSCs were co-cultured with the sterilized 3D-scaffolds placed in transwells for 14 days. The alkaline phosphatase (ALP) activity in the cell lysates was measured using ALP Assay Kit (QuantiChromeTM, BioAssay Systems, Hayward, CA). After fixation and permeabilization, the rBMSCs were stained with rabbit polyclonal *anti*-osteopontin (OPN) antibody (1:100 dilution; Abcam, Cambridge, UK) overnight. After washing, the cells were further stained with goat anti-rabbit IgG Alexa Fluor® 488 secondary antibody (1:1000 dilution), rhodamine-phalloidin (1:200 dilution), and DAPI, then observed using the confocal microscope.

2.7. Immuno-functionalization of 3D-scaffolds

The 3D-printed scaffolds (3D-Scaf) and 2D material-functionalized 3D-Scaf-BP, 3D-Scaf-GO, and 3D-Scaf-GOBP scaffolds were immersed in rat IL-4 solution (1 μg/mL; Sigma Aldrich) overnight to allow protein adsorption. The scaffolds with IL-4 cytokines were then dried under vacuum to obtain 3D-Scaf-Immuno, 3D-Scaf-BP-Immuno, 3D-Scaf-GO-Immuno, and 3D-Scaf-GOBP-Immuno scaffolds, respectively. Loading amounts and release kinetics from these immuno-functioned scaffolds were performed using the rat IL-4 ELISA Kit (Sigma Aldrich, Milwaukee, WI) following the manufacturer's instructions.

2.8. Macrophage adhesion to the 3D-Immuno scaffolds

Rat bone-marrow-derived macrophages (rBMDMs, Cell Biologics, Chicago, IL) were expanded in complete macrophage medium added with supplement kit (Cell Biologics) containing granulocyte-macrophage colony-stimulating factor (GM-CSF), fetal bovine serum (FBS) and penicillin-streptomycin. When reaching 80% confluency, the macrophages were scratched off and seeded onto sterilized immuno-functioned 3D-scaffolds at a density of 100,000 per scaffold. The adhered rBMDM numbers on these scaffolds at 12, 24, and 72 h post-seeding were tested by MTS assay with absorbance read at 490 nm. For immuno-fluorescence staining, rBMDMs on the immuno-functioned 3D-scaffolds were fixed, permeabilized, stained with rhodamine-phalloidin and DAPI, then imaged on the confocal microscope.

2.9. Flow cytometry

For flow cytometry analysis, the macrophages were seeded onto sterilized immuno-functioned 3D-scaffolds. After 3 days of culture, the rBMDMs were collected and stained with rabbit polyclonal anti-CD206 (Abcam, Cambridge, UK) and mouse monoclonal anti-CD68 (Abcam) for 1 h. Then the cells were centrifuged to remove extra antibodies, and stained with Alexa Fluor 488 anti-rabbit IgG secondary antibody (Abcam) and Alexa Fluor 647 anti-mouse IgG secondary antibody (Abcam) for 30 min. The expression of CD68 and CD206 on the rBMDMs growing on the immuno-functioned 3D-scaffolds was analyzed by a flow cytometer.

2.10. Immunofluorescence staining of macrophage phenotypic markers

For phenotype analysis, the macrophages were co-cultured with the sterilized immuno-functioned 3D-scaffolds placed in transwells for 3 days. After fixation and permeabilization, the rBMDMs were stained with *anti*-iNOS antibodies (Abcam), anti-CD68 antibodies (Abcam), and DAPI, then observed on the confocal microscope to determine M1 phenotypic ratio. With the same process, rBMDMs were stained with anti-CD206 antibodies, anti-CD68 antibodies, and DAPI to determine the M2 phenotypic ratio. Immunofluorescence images were obtained on a confocal microscope, and the ratios of $CD206^+$ macrophage and $iNOS^+$ macrophages were analyzed.

2.11. Macrophage medium on vascularization and osteogenesis induction

For vascularization induction ability analysis, primary human umbilical vein endothelial cells (HUVEC, ATCC, Manassas, VA) were expanded in vascular cell basal medium (ATCC, Manassas, VA) supplemented with 2% fetal bovine serum, 0.5% penicillin−streptomycin, 50 μg/mL ascorbic acid, recombinant human insulin-like growth factor (rhIGF-1, 15 ng/mL), recombinant human epidermal growth factor (rhEGF, 5 ng/mL), recombinant human vascular endothelial growth factor (rhVEGF, 5 ng/mL), recombinant human fibroblast growth factor (rhFGF, 5 ng/mL) basic, L-glutamine (10 mM), hydrocortisone (1 μg/mL), and heparin sulfate (0.75 units/mL). The macrophages were first co-cultured with the released medium from immuno-functioned 3D-scaffolds placed in transwells, and the supernatants were then collected and further co-cultured with HUVECs (1:1 medium to supernatants ratio). After 7 days of co-culture, the vascular marker mRNA expressions in the HUVECs were analyzed by real-time PCR using human-specific gene primers (Table S1). The intracellular expression of vascular marker protein CD31 was visualized by immunofluorescence staining using goat anti-CD31 polyclonal primary antibody (Novus Biologicals, CO) and bovine anti-goat IgG CF™633 secondary antibody (Sigma Aldrich).

For osteogenesis analysis, the rBMSCs were added with supernatants from macrophages co-cultured with the released medium from immuno-functioned 3D-scaffolds placed in transwells. After 14 days of co-culture, the osteogenic markers mRNA expressions in the rBMSCs, including osteopontin (OPN), osteocalcin (OCN), runt-related transcription factor 2 (Runx2), and osterix (OSX), were analyzed by real-time PCR using rat-specific gene primers (Table S2). The ALP activity in the cell lysates was tested using ALP Assay Kit. After fixation and permeabilization, the rBMSCs were stained with rabbit polyclonal *anti*-Runx2 antibody (1:100 dilution; Abcam) overnight. After washing, the cells were further stained with goat anti-rabbit IgG Alexa Fluor® 488 secondary antibody (1:1000 dilution), rhodamine-phalloidin (1:200 dilution), and DAPI, then imaged using the confocal microscope.

2.12. Rat calvarial defect model

All animal work in this study was conducted in compliance with the Institutional Animal Care and Use Committee (IACUC) at Mayo Clinic. A Sprague Dawley rat critical-sized cranial defect model was used for *in vivo* bone regeneration evaluation of the 3D-scaffolds. Two full-thickness defects with 5-mm diameter were created. The calvarial defects were either left untreated (control groups) or implanted with one of eight 3D-scaffolds (experimental groups). The skin was then closed with 4.0 vicryl sutures. Each group in the study was explored by three replicates. At 4 weeks post-surgery, the rats were euthanized, and the skull pieces were cut off and soaked in 10% PFA solution for 1 day before scanning on a μ-CT system (Bruker Skyscan 1276, Germany). 3D reconstruction of bone images with quantitative analysis of the bone volume to tissue volume (BV/TV) ratio, bone mineral density (BMD), and new bone area were calculated using the micro-CT system software.

2.13. In vivo osteogenesis and neovascularization

For immunohistochemistry (IHC) analysis, the skull specimens were decalcified using histological decalcifying solution containing EDTA and hydrochloric acid. Tissue sections were sliced after embedding in paraffin, and stained with H&E, Masson trichrome, and toluidine blue. Histological images of bone defect tissue slices were obtained by a slide scanner. To exam the *in vivo* osteogenesis and neovascularization in the rat calvarial defect site, immunofluorescence double-staining was conducted by incubating tissue slices with anti-ALP-Alexa Fluor 488 (1:200 dilution, Novus Biologicals) and anti-CD31-Alexa Fluor 594 (1:200 dilution, Novus Biologicals) for 4 h at 37 °C with protection from light. After final staining with DAPI for 5 min, the immune-fluorescence labeled tissue slices were imaged using a slide scanner.

2.14. *In vivo* M2 macrophage phenotype

To explore the *in vivo* M2 macrophage phenotypes in the rat calvarial defect site, the bone slices were immunofluorescence double-stained with rabbit polyclonal anti-CD206 and mouse monoclonal anti-CD68 overnight at 4 °C. The slices were then washed 3 times to remove extra antibodies, and stained with anti-rabbit IgG-Alexa Fluor 488 secondary antibody and anti-mouse IgG-Alexa Fluor 647 secondary antibody for 1 h at 37 °C. After final staining with DAPI for 5 min, the images of immune-fluorescence labeled tissue slices were acquired using a slide scanner. The intensity of CD206 and CD68 in the defect sites was

analyzed using the ImageJ software (National Institutes of Health).

2.15. Statistical analysis

The statistical differences among experimental groups were tested by one-way analysis of variance (ANOVA) with further Tukey post-test when necessary. Two experimental groups with p-value tested lower than 0.05 was noted as significantly different.

3. Results

3.1. Hetero-nanostructures synthesis

TEM and SEM microscopy confirmed the production of small BP nanosheets with size ranges in the nanometer scale after sonication (Fig. 2a and Fig. S1a). Detailed view of these images clearly demonstrated the exfoliated layers on the BP nanosheets, consistent with previous references. [52,56] Further AFM test detected a layer height in a range of 30–40 nm after exfoliation (Fig. 2b), indicating a multi-layer structure for the exfoliated BP nanosheets, as previously reported [52, 56]. TEM images confirmed the generation of GO nanosheets after oxidation and exfoliation (Fig. 2c). Further AFM test detected a height around 1–2 nm (Fig. 2d), which is close to the thickness of a single GO layer [50], indicating that single layer of GO was obtained after oxidation and exfoliation.

After mixing the GO nanosheets and BP nanosheets, hetero-nanostructures containing both layers of the two 2D materials were obtained. As shown in Fig. 2e, TEM images demonstrated that BP nanoflakes were homogeneously distributed with the GO nanosheets. Detailed visualization of GOBP hetero-nanostructures showed that BP nanoflakes were thoroughly wrapped by a large area GO layers. These characterizations indicated that the two types of 2D materials, BP nanosheets, and GO nanosheets, are not exclusive of each other and thus can be successfully applied to form hetero-nanostructures (Fig. 2f).

3.2. 3D printing and functionalization of polymer scaffolds

Polymeric 3D scaffolds in the dimension of 30 × 30 × 1 mm (length × width × height) were printed on a Bio-X printer, with infill density set as 50% and ink diameter at 400 μm, as shown in Fig. 2g. In order to make suitable scaffolds for cell study and animal implantation, round 3D-scaffold specimens were further punched out using a biopsy punch with 4.5 mm in diameter. The obtained 3D-scaffolds were immersed in solutions with various 2D materials, i.e., GO nanosheets, BP nanosheets, and GOBP hetero-nanostructures for surficial functionalization (Fig. 2h). After drying, the scaffolds with sole 2D BP nanosheet materials showed slight grey to light dark colors, while the scaffolds with 2D GO nanosheet had a darker appearance (Fig. 2i). The 3D-scaffolds with 2D GOBO hetero-nanostructures showed essential 2D materials on the surface with dark color (Fig. 2i). Schematic demonstration of the 4 types of scaffolds were shown in Fig. 2j, namely 3D-Scaf, 3D-Scaf-BP 3D-Scaf-GO, and 3D-Scaf-GOBP, respectively.

SEM microscopy of the 3D-scaffolds showed the corresponding features of 2D materials on the surface of polymer scaffolds at the nanoscale (Fig. 2k-l). For 3D-printed scaffolds without deposition of 2D materials, the scaffold surface is smooth without debris. After coating with a layer

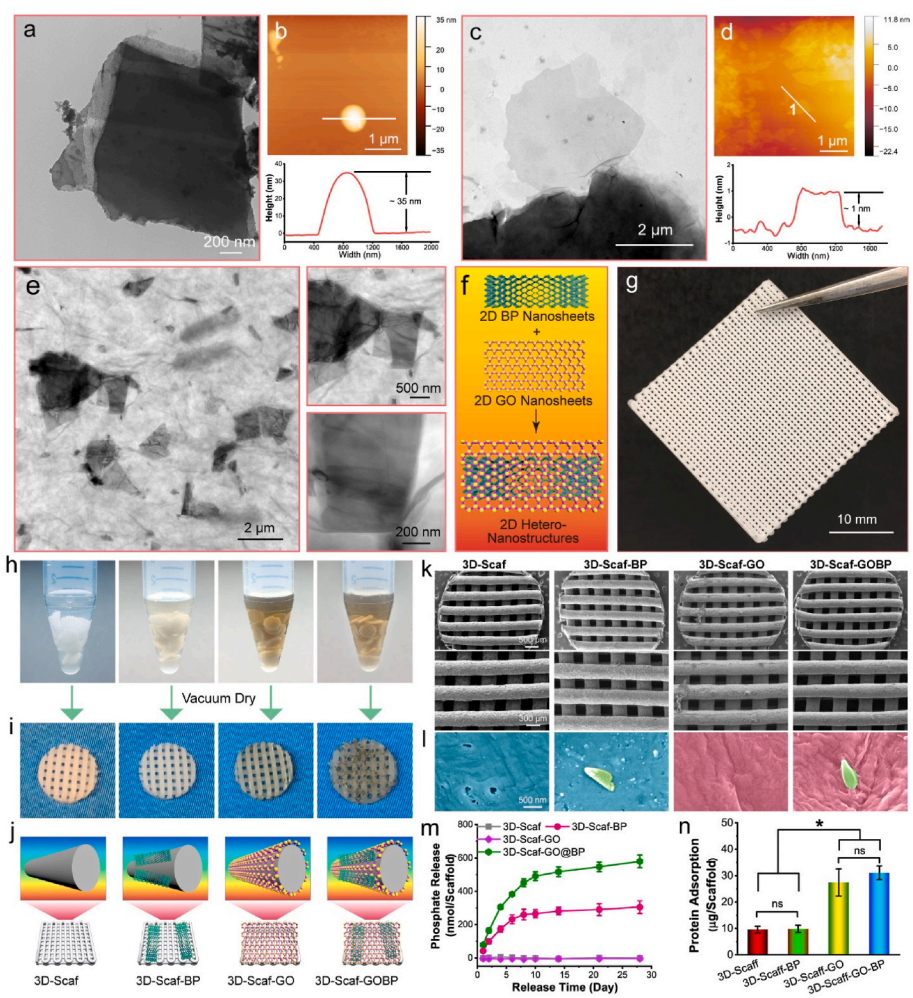

Fig. 2. Scaffolds Characterization. a) TEM images and b) AFM characterization of BP nanosheets. c) TEM images and d) AFM characterization of GO nanosheets. e) TEM images and f) schematic demonstration of 2D hetero-nanostructures formed by GO nanosheets and BP nanosheets. g) Photograph of a 3D printed polymer sheet and h) the punched 3D scaffolds immersed in pure DI H_2O solutions and solutions containing 2D BP nanosheets, GO nanosheets, or GOBP hetero-nanostructures for surficial functioning. i) Photographs and j) schematic demonstrations of the resulting 4 types of 3D scaffolds: plain scaffolds (3D-Scaf), scaffolds functionalized with 2D BP nanosheets (3D-Scaf-BP), GO nanosheets (3D-Scaf-GO), and GOBP hetero-nanostructures (3D-Scaf-GOBP). k) SEM images of the 3D scaffolds and scaffolds functionalized with 2D materials. l) Enlarged view of the surface morphology of the 4 types of 3D scaffolds with detailed indication of the polymer surface (cyan), BP nanosheets (green), and GO nanosheets (pink). m) Cumulative phosphate ion release profile and n) protein adsorption ability for the various functionalized 3D scaffolds. (*: $p < 0.05$; ns: not significant).

of 2D BP nanosheets, the obtained 3D-Scaf-BP scaffolds had a coating of BP nanoflakes dispersed randomly on the surfaces, as indicated by the green color in Fig. 2l. After coating with a layer of 2D BP nanosheets, the obtained 3D-Scaf-GO scaffolds were fully covered with a thin layer of GO nanosheets on the top of all the scaffolds surfaces. For 3D-Scaf-GOBP scaffolds coated with GOBP hetero-nanostructures, the surfaces were fully covered in abundance GO layer with BP nanoflakes randomly embedded within the layer. These results indicate that GO has a larger area and higher affinities for the 3D-scaffolds as compared to BP nanoflakes. The application of GOBP hetero-nanostructures allows better deposition of BP nanoflakes onto the 3D-scaffolds by encapsulating them within 2D GO layers with large surface areas.

The BP nanosheets can be oxidated slowly by reacting with oxygen and water to release phosphate ions continuously. As shown in Fig. 2m, the phosphate ions were intensively released from 3D-Scaf-BP scaffolds by oxidation in the first 6–8 days after immersion in the releasing medium. Afterwards, the release profile reached a plateau, with no significant release of phosphate ions was observed till 28 days. For 3D-Scaf-GOBP scaffolds, the burst release occurred in the first 8–10 days, with a slow continuous release of phosphate ions throughout the observation time period. This difference may be originated from the reduced oxidation of phosphates after they are encapsulated within the GO layer, which may diminish the access of H_2O and O_2 to embedded BP nanosheets, thus attenuating the oxidation process [57]. Water contact angle measurements showed that the functioning with 2D materials slightly altered the substrate surface hydrophilicity, potentially due to the hydrophilic natures of graphene oxide and oxidated phosphate ions from black phosphorus (Fig. S1b).

Protein adsorption tests showed that the 3D-scaffolds functionalized with 2D GO nanosheets or GOBP hetero-nanostructures adsorbed significantly higher amount of proteins to the surface, as compared with the other two groups (Fig. 2n). The robust adsorption of proteins was widely reported for GO nanosheets in previous reports [58,59]. The possible mechanism may be due to the exceptionally large surface area of the GO nanosheets, as well as possible ionic bonding between the amino acids and the –OH and –COOH functional groups of GO nanosheets [60,61].

3.3. Stem cell proliferation and osteogenesis

The biocompatibility of the 2D material functionalized 3D-scaffolds is pivotal for *in vivo* implantation. As shown in Fig. 3a, the live/dead staining indicated most of the rBMSCs attached to the four types of 3D-scaffolds were kept in a live state after 3 days. In comparison to the unfunctionalized pure 3D-scaffolds, the 3D-Scaf-BP and 3D-Scaf-GO, which functionalized with 2D BP nanosheets or GO nanosheets, showed denser cell adhesion on the surface. For 3D-Scaf-GOBP coated with GOBP hetero-nanostructures, the highest cell numbers were observed and the cells covered largely the entire scaffold surface. Along with the direct contact adhesion of cells onto the scaffolds, the cytotoxicity of leaching media from the 3D-scaffolds were also evaluated. As can be noted from Fig. 3b, no significant influence of leaching media on the viability of co-cultured stem cells was noted after 3 and 7 days. These results indicate that the functionalized 3D-scaffolds are not cytotoxic to stem cells and not releasing toxic substances to the media and therefore biocompatible and applicable for *in vitro* cell study and *in vivo* implantation.

To evaluate the proliferation of stem cells, rBMSCs were seeded on to these 3D-scaffolds. As can be seen from Fig. 3c, stem cells showed a growing trend on all 4 types of 3D-scaffolds, similar to the TCPS control.

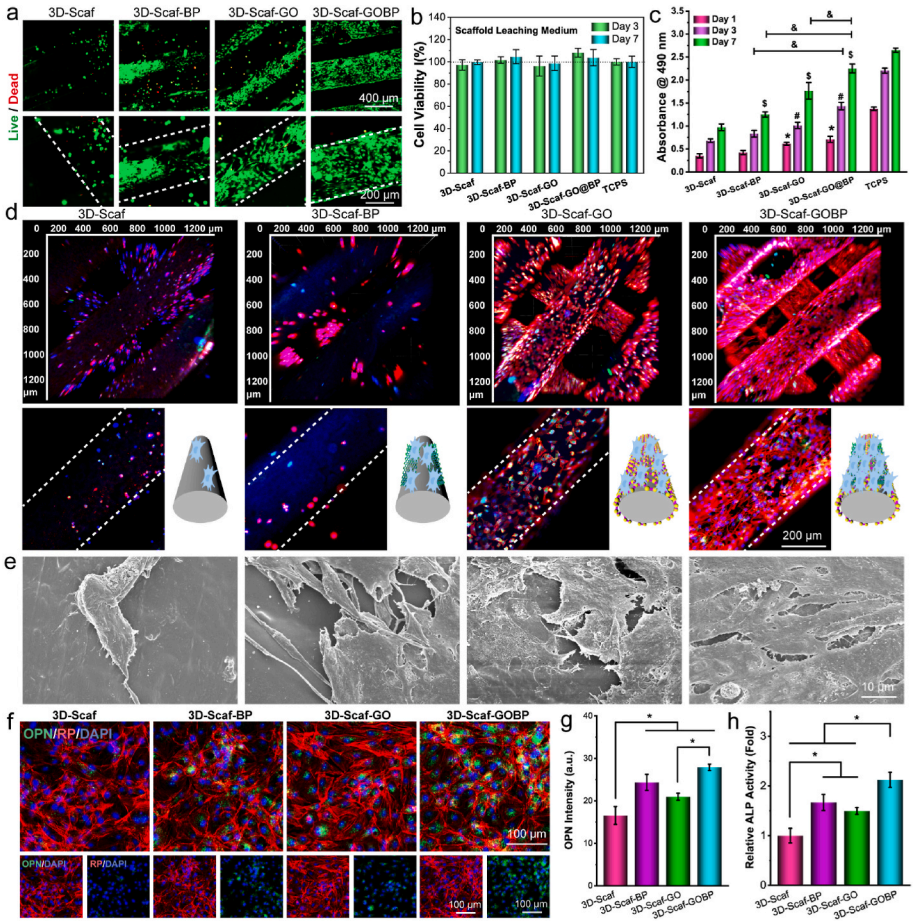

Fig. 3. Stem cell behavior on the scaffolds. a) Live/dead staining of rBMSCs after 7 days of growing on the pure 3D scaffolds and scaffolds functionalized with GO nanosheets, BP nanosheets, and 2D hetero-nanostructures formed by GO and BP nanosheets. b) Stem cell viability after co-culture with leaching medium from these functionalized 3D scaffolds. c) Proliferation of stem cells at 1, 3, 7 days post-seeding on these 3D scaffolds (*, $, #: $p < 0.05$ to control group; &: $p < 0.05$). d) Immunofluorescence imaging (red: F-actin; green: vinculin; blue: DAPI) and e) SEM imaging of stem cells on these 3D scaffolds after 7 days. f) Confocal imaging of immunofluorescence-stained osteogenic marker OPN (green: OPN; red: F-actin; blue: DAPI), g) quantified OPN intensities, and h) ALP activities in stem cells after 14 days of culture in leaching medium from functionalized 3D scaffolds (*: $p < 0.05$).

After 7 days, the 2D material functionalized 3D-scaffolds showed a significantly higher number of cells proliferated than the pure 3D-scaffolds. For visualization of morphological features on the 3D-scaffolds, stem cells were stained with immunofluorescence *anti*-vinculin−FITC antibody, rhodamine-phalloidin, and DAPI, then imaged by confocal microscope. As presented in Fig. 3d, the reconstructed 3D-scanning confocal images showed abundant of stem cells adhered to the top and inside ridges of 3D-scaffolds that were functionalized with 2D GO nanosheets or GOBP hetero-nanostructures. In contrast, for unfunctionalized pure 3D-scaffolds and the 3D-Scaf-BP functionalized with 2D BP nanosheets, cell densities were remarkably lower. After critical point drying, the SEM images of the stem cells showed a consistent trend with abundant cells on the 2D nanosheets, and hetero-nanostructures functionalized 3D-scaffolds as compared to the unfunctionalized pure 3D-scaffolds (Fig. 3e, Fig. S2).

This result implies that the function of GO layers distinctly facilitates the cell adhesion ability to the 3D-scaffold surfaces, consistent with previous reports of improved cell proliferation after carbon material functionalization [24]. Among the four groups, the most robust adhesion and proliferation of stem cells were observed on the 3D-Scaf-GOBP scaffolds functionalized with GOBP hetero-nanostructures. An enlarged view of single scaffolds ridges revealed stem cells covering almost the entire surface areas of the 3D-Scaf-GOBP scaffolds. These results denote that the function of GOBP hetero-nanostructures may receive a synergistic enhancement effect from the two nanomaterials, taking advantage of the large surface area of 2D GO nanosheets and the desired continuous release of phosphate ions from the 2D BP nanosheets.

To confirm the effect of 3D-scaffolds in inducing osteogenesis of stem cells, the releasing media from the different scaffolds were collected and co-cultured with the stem cells at the same seeding density and culture conditions. After 14 days of culture, the expression of osteogenic maker protein OPN was visualized by immunofluorescence staining. As shown in Fig. 3f, the stem cells all showed expression of OPN protein after 14 days. The cells cultured with releasing media from 3D-Scaf-GOBP scaffolds, however, displayed a relatively higher OPN content (green fluorescence). The quantification of fluorescence intensities of OPN protein confirmed significantly higher values for cells cultured with releasing media from 3D-Scaf-GOBP scaffolds (Fig. 3g). In addition, the relative ALP activity tests showed significantly higher levels in cells cultured with 3D-scaffolds functionalized with 2D materials, as compared to the unfunctionalized pure 3D-scaffold (Fig. 3h). These results indicate that the 2D GO nanosheets and the phosphate ions released from the functionalized scaffolds could facilitate cell osteogenesis.

3.4. Immuno-function of 3D-scaffolds and macrophage response

The unfunctionalized pure 3D-scaffolds and the 2D material functionalized 3D-scaffolds were all immersed in rat IL-4 solution to allow adsorption of IL-4 cytokines (Fig. 4a). After drying, 3D-scaffolds with immunological IL-4 cytokines were obtained, namely 3D-Scaf-Immuno, 3D-Scaf-BP-Immuno, 3D-Scaf-GO-Immuno, and 3D-Scaf-GOBP-Immuno scaffolds. As shown in Fig. 4b, the IL-4 loading content was significantly higher on the 3D-Scaf-GO-Immuno and 3D-Scaf-GOBP-Immuno scaffolds pre-functionalized with GO layers or GOBP hetero-nanostructures, respectively, as compared to 3D-Scaf-Immuno without pre-functionalization and 3D-Scaf-BP-Immuno pre-functionalized with BP nanosheets. Release kinetics study showed that the 3D-Scaf-Immuno and 3D-Scaf-BP-Immuno had burst release of IL-4 cytokines in the first 2 days, then reached a plateau, and no large-scale release was detected thereafter (Fig. 4c). For 3D-Scaf-GO-Immuno and 3D-Scaf-GOBP-

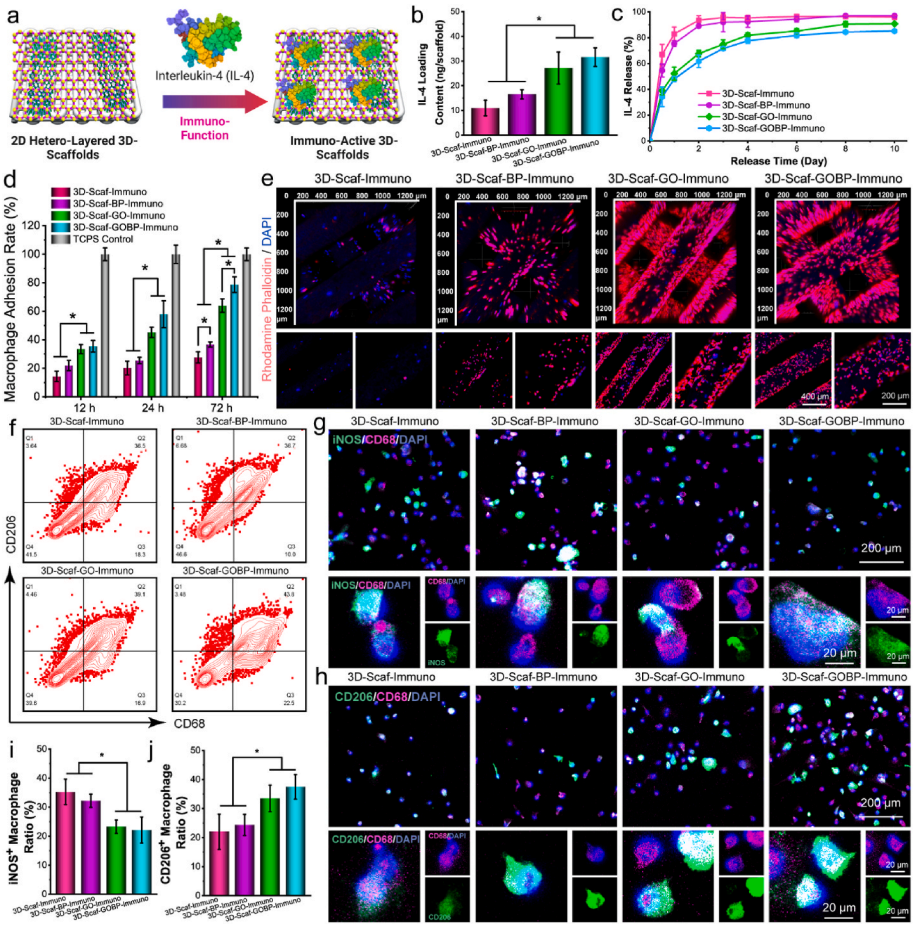

Fig. 4. Immuno-functionalization and macrophage phenotype shift. a) Schematic demonstration of the immuno-functionalization of IL-4 cytokines to the 3D scaffolds. b) IL-4 loading content and c) IL-4 release profiles of the 3D scaffolds functionalized with 2D materials. d) Macrophage adhesion rates and e) immunofluorescence imaging of macrophages attached to the 3D scaffolds after immuno-functionalization. f) Flow cytometry analysis of macrophage phenotypes after staining with CD68 and CD206 antibodies. Confocal imaging of macrophages after immunofluorescence staining with g) M1 phenotypic marker antibodies (iNOS) and h) M2 phenotypic marker antibodies (CD206), together with a pan-macrophage marker (CD68) and DAPI. Quantitative analysis of i) iNOS$^+$ cell ratio and j) CD206$^+$ cell ratio after co-culture with leaching medium from immuno-functionalized 3D scaffolds. (*: $p < 0.05$).

Immuno scaffolds, the release profile was determined to have a smaller burst release in the first 4 days, then slow continuous release of the IL-4 cytokines throughout the 10-day period.

The adhesion of bone marrow derived macrophages (rBMDMs) to the sterilized immuno-functioned 3D-scaffolds was tested at 12, 24, and 72 h post-seeding. As presented in Fig. 4d, at 12 h post-seeding, the 3D-Scaf-GO-Immuno and 3D-Scaf-GOBP-Immuno scaffolds showed immediately higher attraction of macrophages to the surface. After 72 h, all three scaffolds pre-functionalized with 2D materials, i.e., 3D-Scaf-BP-Immuno, 3D-Scaf-GO-Immuno, and 3D-Scaf-GOBP-Immuno scaffolds, all had significantly higher adhesion of macrophages as compared to the non-pre-functionalized 3D-Scaf-Immuno scaffolds (Fig. 4d). The 3D-Scaf-GOBP-Immuno scaffolds had the highest number of macrophages, demonstrating the best properties for macrophage attraction and proliferation.

The immuno-fluorescence images showed consistent results, with 3D-Scaf-GO-Immuno and 3D-Scaf-GOBP-Immuno scaffolds gathering a higher number of macrophages to the surface compared to the other scaffolds (Fig. 4e). Enlarged view of the polymeric ridges in the 3D-scaffolds showed much denser macrophage distribution on the 3D-Scaf-GO-Immuno and 3D-Scaf-GOBP-Immuno scaffolds, covering large areas of the ridges. In addition, the macrophages were visualized to have better-spread morphology. As a comparison, the macrophages on the 3D-Scaf-Immuno and 3D-Scaf-BP-Immuno showed sparse distribution profiles with round dot-shaped morphology, demonstrating non-optimized surfaces for these 3D-scaffolds (Fig. 4e).

Macrophage phenotype changes in response to immuno-functioned 3D-scaffolds were characterized. Macrophages growing on the immuno-functioned 3D-scaffolds were collected and immunolabeled with CD68 and CD206, an M2 macrophage-specific marker. Flow cytometry analysis showed $CD206^+$ macrophages were detected on all four types of immune-functionalized 3D-scaffolds, indicating the IL-4 loading induced the polarization of macrophages toward M2 phenotype (Fig. 4f). Furthermore, the ratio of $CD206^+$ macrophages on the 3D-Scaf-GOBP-Immuno scaffolds was higher than the other three types of scaffolds (Fig. 4f), demonstrating that the improved IL-4 cytokine loading and release via hetero-nanolayers could achieve potent phenotype polarization of macrophages after adhering to the 3D-scaffolds.

In addition to direct co-culture, the phenotype shifts in macrophages in responding to the leaching media from the immune-functionalized 3D-scaffolds were also characterized. After co-culture with the sterilized immuno-functioned 3D-scaffolds placed in transwells for 3 days, macrophages were immune-labeled with either CD68 with iNOS, an M1 phenotypic marker, or CD68 with CD206, an M2 phenotypic marker. As presented in Fig. 4g, the immunolabeling of M1 phenotypic marker iNOS showed more notable fluorescence from the macrophages co-cultured with the 3D-Scaf-Immuno scaffolds. For 3D-Scaf-GO-Immuno and 3D-Scaf-GOBP-Immuno scaffolds that were pre-functionalized with GO layers and GOBP hetero-nanostructures, respectively, and loaded with a significant content of IL-4 cytokines, the iNOS fluorescence was reduced, indicating a lowered polarization of macrophages into M1 phenotype (Fig. 4g, Fig. S3). On the contrary, for M2 phenotypic marker CD206 staining, more robust fluorescence was observed for 3D-Scaf-GO-Immuno and 3D-Scaf-GOBP-Immuno scaffolds (Fig. 4h, Fig. S4). Enlarged view of single macrophages also visualized the distribution of CD206 fluorescence across the macrophage cell body.

Quantitative analysis of $iNOS^+$ cell ratio showed a decreased trend for M1 phenotypes for macrophages cultured with 3D-Scaf-GO-Immuno and 3D-Scaf-GOBP-Immuno scaffolds, while the quantification of $CD206^+$ cell ratio showed an increasing trend for M2 phenotypes for macrophages cultured on these two types of scaffolds. In correlation with the highest IL-4 loading content and robust macrophage attraction on the 3D-Scaf-GOBP-Immuno scaffolds, this macrophage M2 phenotype polarization may be originated from the dense gathering of macrophages followed by potent polarization induced by a large amount of IL-4 cytokines. Taken together, all these results imply that the 2D materials with a large surface area for macrophage affinity could effectively enhance the attraction of macrophages to 3D-scaffolds, and further improve the loading of phenotypic modulation markers to induce macrophages into the desired phenotype.

3.5. Macrophage effect on vascularization and osteogenesis

To explore whether macrophages in response to immuno-functioned 3D-scaffolds could influence the vascularization and osteogenesis of adjacent cells, the releasing medium from macrophages was co-cultured with HUVECs and rBMSCs. The macrophages were co-cultured with releasing medium from immuno-functionalized 3D-scaffolds, and the supernatants were then further cultured with either HUVEC or rBMSCs, as schematically demonstrated in Fig. 5a.

After co-culture for 7 days, the vascular markers mRNA expressions in the HUVECs, including angiopoietin-1 (ANG1), basic fibroblast growth factor 2 (bFGF2), endothelial nitric oxide synthase 3 (eNOS3), vascular endothelial growth factor A (VEGFA), vascular endothelial growth factor C (VEGFC), were analyzed by real-time PCR. As presented in Fig. 5b–f, the relative mRNA expressions varied for different genes. However, a general trend with higher expressions of vascular genes was detected in HUVECs co-cultured with supernates from macrophages induced by IL-4 cytokines from immuno-functionalized 3D-scaffolds. This is especially obvious for the 3D-Scaf-GOBP-Immuno scaffolds that were pre-functionalized with hetero-nanostructures and loaded with high content of IL-4 cytokines, which showed the highest expression of these vascular genes.

The intracellular CD31 protein, a vascular marker, was visualized by immunofluorescence staining. As shown in Fig. 5g, the fluorescence intensities of the CD31 were quantified to have the highest values in HUVECs co-cultured with supernates from macrophages induced by 3D-Scaf-GOBP-Immuno scaffolds leaching medium. Typical confocal images with the staining of CD31 marker protein showed CD31 protein was distributed sparsely in HUVECs co-cultured with supernates from macrophages induced by leaching medium from pure 3D-Scaf-Immuno scaffolds (Fig. 5h, Fig. S5). As a comparison, CD31 was observed to be expressed and distributed across the cytoplasm of HUVECs co-cultured with supernates from macrophages induced by leaching medium from 3D-Scaf-GOBP-Immuno scaffolds.

For osteogenesis analysis, rBMSCs were added with macrophage supernatants after co-culture with releasing medium from immuno-functioned 3D-scaffolds. After 14 days, the mRNA expressions of osteogenic markers, including osteopontin (OPN), osteocalcin (OCN), runt-related transcription factor 2 (Runx2), and osterix (OSX), were analyzed by real-time PCR. Results showed a similar trend to the vascular markers where the highest value was detected for rBMSCs co-cultured with supernates from macrophages induced by leaching medium from 3D-Scaf-GOBP-Immuno scaffolds (Fig. 5i-l). The ALP activities in the cell lysates were detected to be significantly higher in rBMSCs co-cultured with macrophage supernates induced by 3D-Scaf-BP-Immuno scaffolds, 3D-Scaf-GO-Immuno scaffolds, and 3D-Scaf-GOBP-Immuno scaffolds, as compared to that of the pure 3D-Scaf-Immuno scaffolds (Fig. 5m).

Runt-related transcription factor 2 (Runx2) is a transcription factor that plays critical roles in cell osteogenesis, bone matrix protein expression, cartilage, and bone development [62–64]. The expression of Runx2 osteogenic protein was labeled by immunofluorescence staining. As compared with rBMSCs exposed to macrophage supernates induced by pure 3D-Scaf-Immuno scaffolds, all other three groups showed higher fluorescence intensities of the Runx2, an osteogenic marker protein (Fig. 5n). Typical confocal images showed OPN marker protein were intensively expressed in rBMSCs after exposure to macrophage supernates after induction with leaching medium from 3D-Scaf-GOBP-Immuno scaffolds (Fig. 5o).

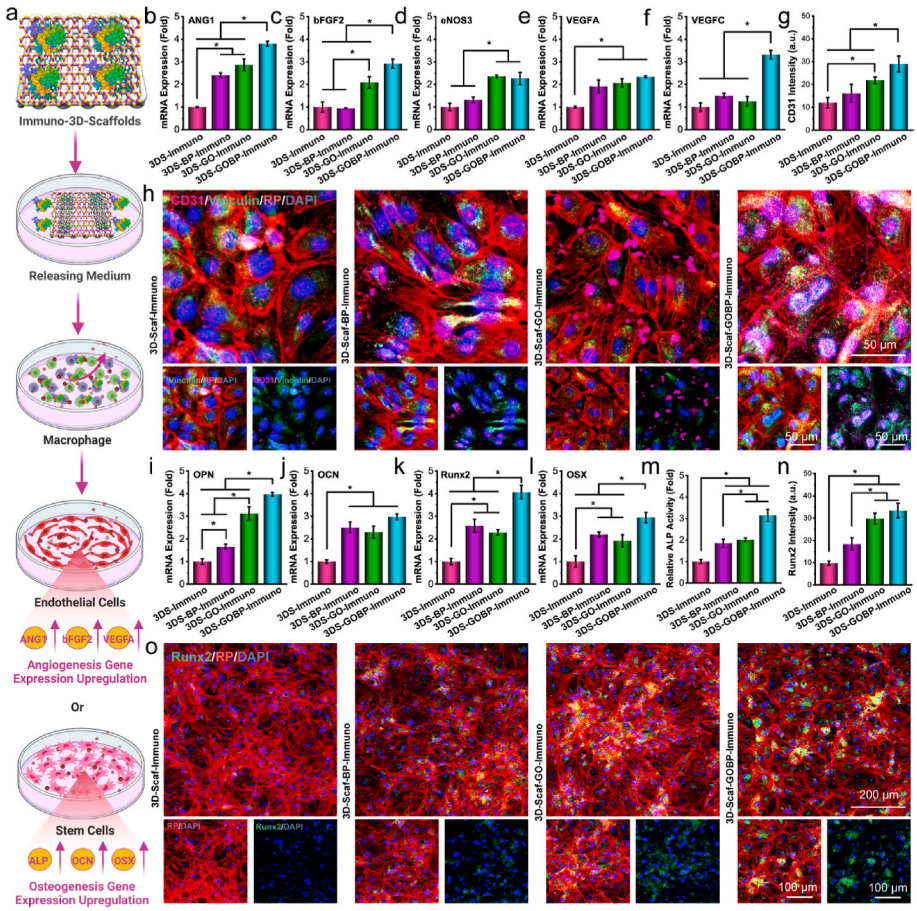

Fig. 5. The *in vitro* vascularization and osteogenesis. a) Schematic demonstration of the co-culture of macrophages in IL-4 released medium from the immuno-functionalized 3D scaffolds and the subsequent induction of vascularization for HUVEC cells or osteogenesis for rBMSCs using the supernatant from the macrophage co-culture. Relative mRNA expressions of b) ANG1, c) bFGF2, d) eNOS3, e) VEGFA, and f) VEGFC vascular marker genes in HUVECs. g) Fluorescence intensities of the CD31 vascular marker and h) confocal images of HUVECs stained immunofluorescent with CD31 (pink), F-actin (red), vinculin (green), and nuclei (blue: DAPI) after co-culture with macrophage supernatant. Relative mRNA expressions of i) OPN, j) OCN, k) Runx2, and l) OSX osteogenic marker genes in rBMSCs. m) Relative ALP activities, n) fluorescence intensities of Runx2, and o) confocal images of rBMSCs stained with immunofluorescent F-actin (red), Runx2 (green), and nuclei (blue: DAPI) after co-culture with microphage supernatant. (*: $p < 0.05$).

3.6. *In vivo bone regeneration of 3D-Immuno scaffolds*

At bone defect site, the injury microenvironment niche involves various cells and factors (Fig. 6a). The *in vivo* behavior of the various types of 3D-scaffolds in response to the bone injury microenvironment niche and their capability to support bone repair was studied using a rat calvarial defect model. Full-thickness bone defects with a diameter of 5-mm were created and the 3D-scaffolds were implanted into the defect (Fig. 6b). After 4 weeks, the skull pieces were harvested for analysis of bone formation (Fig. 6c–d). As shown in Fig. 6e, the micro-CT images indicated more notable new bone formation within defect sites that were implanted with 3D-scaffolds, as compared to the empty control, which had minimal new bone formation. A detailed view of the defect sites showed that the 3D-scaffolds formed disconnected small bone pieces sparsely disturbed within the bone defect.

For the three types of 3D-scaffolds functionalized with 2D materials, i.e., 3D-Scaf-BP, 3D-Scaf-BP, and 3D-Scaf-GOBP, there were small-scale intact bone pieces formed along the edge of the defect (Fig. 6e). In addition to the intact bone pieces, several disconnected small bone pieces sparsely disturbed within the bone defect were observed, mostly within the pores of the 3D-scaffolds. In comparison, for the four types of immuno-functionalized 3D-scaffolds, i.e., 3D-Scaf-Immuno, 3D-Scaf-BP-Immuno, 3D-Scaf-GO-Immuno, and 3D-Scaf-GOBP-Immuno, substantial intact bone pieces were observed within the defect. For 3D-Scaf-GO-Immuno and 3D-Scaf-GOBP-Immuno scaffolds pre-functionalized with GO layers and GOBP hetero-nanostructures, respectively, and loaded with large content of IL-4 cytokines, the bone defect was largely filled with new bones. There were obvious empty channels within the newly formed bone pieces, which were believed to be the polymer ridges of the 3D-scaffolds.

A quantitative analysis was further conducted based on the micro-CT data to calculate the bone volume to tissue volume (BV/TV) ratio, bone mineral density (BMD), and new bone area. As presented in Fig. 6f–h, these characterizations showed a consistent trend with the micro-CT image analysis. A significantly higher value of BV/TV ratio, BMD, and new bone area, were determined for the 3D-scaffolds, as compared to the empty defect. The highest values for BV/TV ratio, BMD, and new bone area, were tested in the bone defects implanted with 3D-Scaf-GOBP-Immuno scaffolds, which were pre-functionalized with hetero-nanostructures and loaded with high content of IL-4 cytokines. These results indicated that the functionalization of 2D materials on the 3D-scaffolds could enhance new bone formation after *in vivo* implantation. Supplemental immunoregulative cytokine loading could further expedite bone formation.

The H & E staining of major organs (heart, kidney, liver, lung, and spleen) showed no obvious cytotoxicity in rats implanted with pure 3D-scaffolds, 3D-scaffolds with 2D materials, and 3D-scaffolds with 2D materials and IL-4 cytokines, similar to the empty control (Fig. 6i). These results indicated that the 3D-scaffolds used in this study was biocompatible under *in vivo* conditions, consistent with the *in vitro* cell evaluation. The 2D materials used for 3D-scaffold surface functionalization, including BP nanosheets, GO nanosheets, and GOBP hetero-nanostructures, as well as the IL-4 cytokines, were all biocompatible. These functionalized 3D-scaffolds are therefore suitable for *in vivo* implantation without tissue toxicity.

3.7. *In vivo neovascularization and osteogenesis*

To evaluate bone repair with the implanted 3D-scaffolds in the calvarial defect site, the harvested bone tissue was decalcified and sliced after embedding in paraffin. Histological analysis by staining with H&E, Masson trichrome, and toluidine blue were conducted. Fig. 7a–c showed

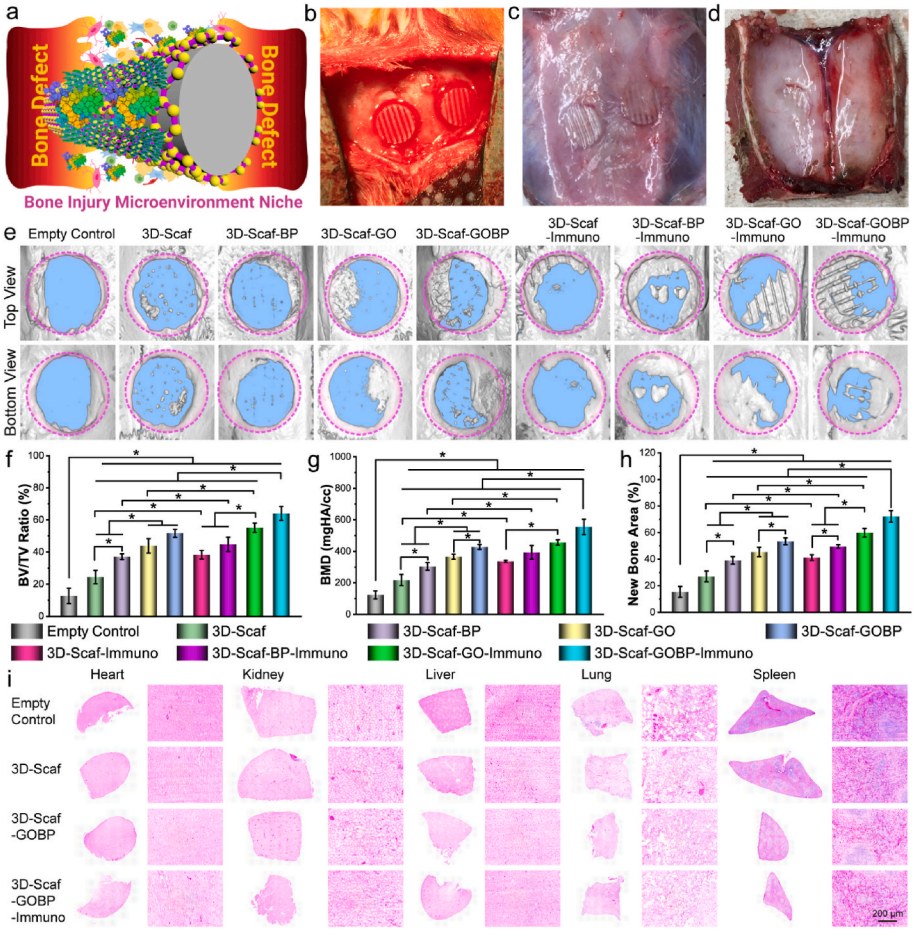

Fig. 6. *In vivo* bone formation of immuno-functionalized scaffolds. a) Schematic demonstration of bone injury microenvironment and cells that will interact with immuno-3D scaffolds after implantation. The photographs of b) initial *in vivo* implantation into the rat calvarial defect and harvest after 4 weeks implantation in the defect sites viewed from the c) top side and d) interior side. e) Micro-CT reconstruction images of the empty rat calvarial defect control and the defects implanted with various scaffolds after 4 weeks of implantation. Quantitative analysis of f) new bone area, g) BV/TV ratio, h) bone mineral density (BMD) in these defects. i) Histological H & E staining of various organs harvested from the rats. (*: $p < 0.05$).

the 3D-scaffolds bridged the bone defect gaps with thick layers of tissue developed on the surface. Further, tissue layers were also observed to penetrate within the pores of the scaffolds. These results indicate that the 3D-scaffolds could bridge the bone defect and provide excellent tissue conductivity for cells to proceed and allocate in the bone defect area.

Within the formed tissues, essential new bone or new bone-like tissues was observed to be developed underneath or on the surface of the 3D-scaffolds in varied patterns. For 3D-Scaf-GO-Immuno and 3D-Scaf-GOBP-Immuno scaffolds pre-functionalized with GO layers and GOBP hetero-nanostructures, respectively, and loaded with large content of IL-4 cytokines, the bone content was noticeably higher than the other groups. In addition, for these two groups, bone pieces were observed within the penetrated tissues and scattered across the 3D-scaffolds. Most of these bone pieces were detected to be allocated within the porotic spaces of the scaffolds. As a comparison, the empty bone defect, which lacks 3D-scaffolds implantation, was observed to be covered with only a thin layer of fibrous tissue, and no essential bone segments were detected across the defect area. These results indicated that the immuno-functionalized 3D-scaffolds could bridge the bone defects and support an osteoconductive environment for cells to allocate, infiltrate, proliferate, and differentiate.

To explore the *in vivo* neovascularization and osteogenesis pattern in the bone defect, the calvarial bones were sliced and immunofluorescent double-stained with CD31 (vascularization marker protein) and ALP (osteogenic marker protein). As presented in Fig. 7d, obvious empty pores were observed for the bone slices implanted with 3D-scaffolds, which were believed to be the polymeric ridges of the scaffolds. In addition, the immunofluorescence images visualized a thicker tissue layer growing on the defects implanted with 3D-scaffolds as compared to the empty bone defect control, demonstrating that scaffold implantation facilitated cell recruitment and tissue formation (Fig. 7d).

For the defects implanted with pure 3D-scaffold, weak ALP and CD31 fluorescence was detected. For the three groups implanted with 2D material functionalized 3D-scaffolds, i.e., 3D-Scaf-BP, 3D-Scaf-GO, and 3D-Scaf-GOBP, relatively stronger ALP and CD31 fluorescence were observed across the top and interior pore areas of the 3D-scaffolds. In comparison, for the four types of immuno-functionalized 3D-scaffolds, i.e., 3D-Scaf-Immuno, 3D-Scaf-BP-Immuno, 3D-Scaf-GO-Immuno, and 3D-Scaf-GOBP-Immuno, noticeable ALP and CD31 fluorescence was detected within the bone defect site (Fig. 7d). It is worth to note that the fluorescence distribution pattern was unique for these 3D-scaffolds. Robust ALP fluorescence was visualized to be surrounding the ridges of the implanted 3D-scaffolds. In parallel, the CD31 fluorescence were largely distributed on the top or bottom of the 3D-scaffolds, as well as in the interior pore areas of the 3D-scaffolds. These results imply that the bone formation was initiated by the cells that were allocated on the ridges of the 3D-scaffolds. Meanwhile, neovascularization was largely developed surrounding the 3D-scaffolds, as well as in the interior part of the scaffolds where large spaces exist.

The immunofluorescence intensities of both ALP and CD31 markers were analyzed. As presented in Fig. 7e, significantly higher ALP intensities ($p < 0.05$) were detected in the bone defects implanted with 3D-scaffolds than the empty defect control. For the three groups implanted with 2D material functionalized 3D-scaffolds, i.e., 3D-Scaf-BP, 3D-Scaf-BP, and 3D-Scaf-GOBP, the ALP fluorescence intensities were stronger than the pure 3D-scaffold. The strongest fluorescence was detected in bone defects implanted with 3D-Scaf-GOBP-Immuno scaffolds pre-functionalized with GOBP hetero-nanostructures and loaded with large content of IL-4 cytokines.

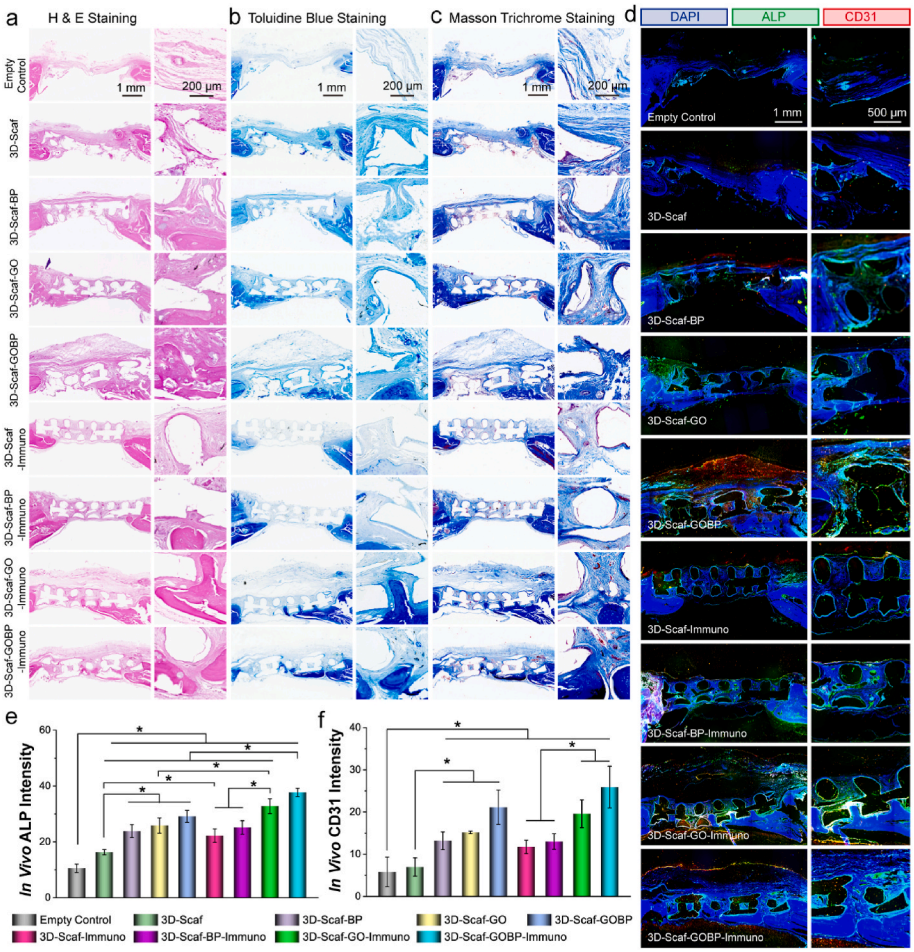

Fig. 7. Immunohistological analysis and *in vivo* neovascularization and osteogenesis in rat calvarial defect model. a) H & E staining, b) toluidine blue staining, and c) Masson's trichrome staining of the empty bone defects and defects implanted with 3D-printed scaffolds. d) Immunohistochemical staining of ALP and CD31 proteins in the empty bone defects and defects implanted with 3D-printed scaffolds. Quantitative analysis of *in vivo* e) ALP and f) CD31 fluorescence intensity in the defect sites. (*: $p < 0.05$).

Quantification of CD31 fluorescence showed a similar trend with enhanced values for defects implanted with 2D material functionalized 3D-scaffolds, as compared to the empty defect and pure 3D-scaffolds (Fig. 7f). After immuno-functionalization, the CD31 intensities elevated slightly. Bone defects implanted with 3D-Scaf-GO-Immuno and 3D-Scaf-GOBP-Immuno scaffolds showed higher CD31 intensities as compared to the 3D-Scaf-Immuno and 3D-Scaf-BP-Immuno scaffolds. The highest CD31 intensity was tested on the bone defects implanted with 3D-Scaf-GOBP-Immuno scaffolds pre-functionalized with GOBP hetero-nanostructures and loaded with large content of IL-4 cytokines. These results indicated that the 3D-scaffolds could bridge the bone defect site and facilitate *in vivo* cell recruitment and osteoconduction. In addition, 3D-scaffolds that were pre-functionalized with 2D hetero-nanostructures and loaded with IL-4 cytokines could further enhance neovascularization and osteointegration and expedite new bone development in the defect area.

3.8. *In vivo M2 macrophage phenotype modulation*

To determine the *in vivo* macrophage recruitment and M2 phenotype polarization in the bone defect, the calvarial bones were immunofluorescent double-stained with CD68 (pan-macrophage marker) and CD206 (M2 macrophage marker). As presented in Fig. 8a, weak CD68 and CD206 immunofluorescence were detected for the empty bone defect. As a comparison, for the bone defect with implanted with pure 3D-scaffold, noticeable fluorescence dots were observed, indicating that the implantation of 3D-scaffolds improved macrophage recruitment (Fig. 8a). For the bone defects implanted with 2D material functionalized 3D-scaffolds, i.e., 3D-Scaf-BP and 3D-Scaf-GO, the CD68 and CD206 fluorescence was observed at low levels, similar to the empty defects and pure 3D-scaffolds (Fig. 8a). For 3D-Scaf-GOBP, a wide distribution of CD68 and CD206 fluorescence was observed within the tissues, indicating the function of hetero-nanostructures could enhance the recruit of macrophages to the 3D-scaffolds.

After immuno-functionalization, recruit and polarization of macrophages were enhanced in general, however, varied for different types of scaffolds. For the 3D-Scaf-Immuno scaffolds that were non-pre-functionalized with 2D materials, the CD68 and CD206 fluorescence did not receive a significant increase. In comparison, for the three types of scaffolds that were pre-functionalized with 2D nanolayers and then immuno-functionalized with IL-4 cytokines, i.e., 3D-Scaf-BP-Immuno, 3D-Scaf-GO-Immuno, and 3D-Scaf-GOBP-Immuno, robust CD68 and CD206 fluorescence was detected within the bone defect site. For the 3D-Scaf-GO-Immuno and 3D-Scaf-GOBP-Immuno scaffolds pre-functionalized with GO layers and GOBP hetero-nanostructures, respectively, and loaded with large content of IL-4 cytokines, the CD68 and CD206 were detected to be the strongest among all the groups.

The immunofluorescence intensities of both CD68 and CD206 proteins were analyzed. As can be noticed from Fig. 8b–c, significantly higher CD68 and CD206 intensities ($p < 0.05$) were detected in bone defects implanted with 3D-Scaf-GOBP than the empty defect and defects implanted with pure 3D-Scaf, 3D-Scaf-GO, 3D-Scaf-BP, consistent with the fluorescence images (Fig. 8b–c). The highest intensities for both CD68 and CD206 protein among all the groups were tested for bone defects implanted with 3D-Scaf-GO-Immuno and 3D-Scaf-GOBP-Immuno scaffolds pre-functionalized with GO layers and GOBP hetero-nanostructures, respectively, and loaded with large content of IL-4 cytokines, consistent with the above fluorescence images.

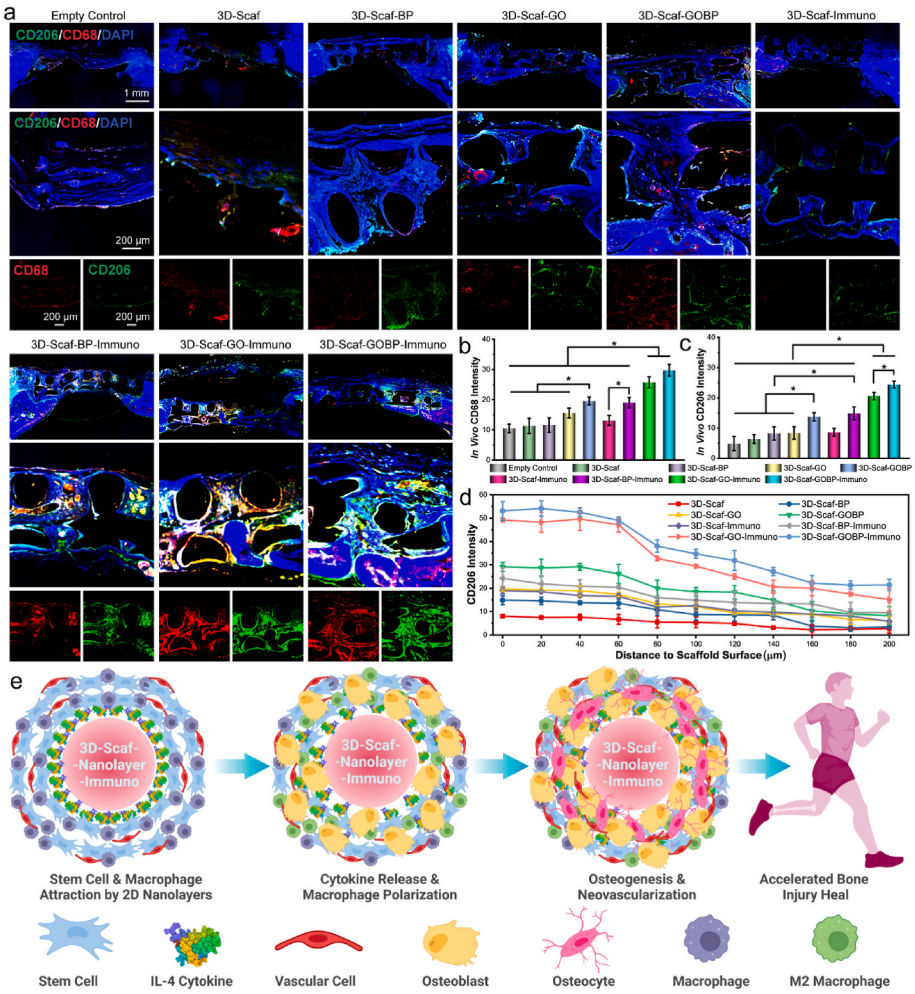

Fig. 8. *In vivo* macrophage phenotype characterization. a) Immunohistochemical analysis of macrophages stained with M2 phenotypic marker antibodies (CD206, green), pan-macrophage marker (CD68, red), and nuclei (DAPI, blue) in tissue slices from the rat defect sites. Quantitative analysis of overall b) $CD68^+$ cell ratio and c) $CD206^+$ cell ratio in tissue slices. d) Fluorescence intensities of CD206 markers at varying distances to the 3D-scaffold ridges. e) Schematic representation of accelerated bone repair via osteo-immunomodulation with the cytokine immuno-functionalized 3D scaffolds. (*: $p < 0.05$).

The *in vivo* distribution of CD206 fluorescence, which indicates the location of polarized M2 macrophages, was unique for these 3D-scaffolds (Fig. 8a). Potent CD206 fluorescence was observed to encircle the implanted 3D-scaffolds ridges. The CD206 fluorescence intensities in relation to the distance to scaffold ridge surfaces were characterized. As shown in Fig. 8d, the CD206 intensities were tested to be the strongest at the tissue-scaffolds interfaces. The intensities reduced in tissues as the distance to the scaffold ridges increased. For tissue layers with a distance greater than 60 μm to the ridge surface, the CD206 intensity dropped noticeably. This outcome may have resulted from the local IL-4 cytokine release from the scaffolds, which induced primarily the adjacent macrophages to polarize into M2 macrophages.

4. Discussion

Overall, these results showed that the 3D-scaffolds could help bridge the bone defect site and assist *in vivo* cell recruitment and tissue formation. In addition, pre-functionalization of the 3D-scaffolds with 2D material layers or 2D hetero-nanostructures could further enhance the neovascularization and osteointegration in the bone defect area, benefitting from the large surface area of GO nanosheets as well as the continuous phosphate release from BP nanosheets. These 2D materials significantly elevated the loading capacity of immuno-active cytokines, e.g., IL-4, to the 3D-scaffolds. After implantation *in vivo*, the IL-4 cytokines could be released from the surface of 3D-scaffolds and delivered to adjacent tissues and stimulate *in vivo* osteo-immunomodulation by polarizing macrophages into a pro-regeneration M2 phenotype. The synergistic effect of continuous phosphate release, which stimulates cell growth, and IL-4 cytokine release, which immune-modulates the injury site into a regeneration-friendly microenvironmental niche, effectively induced neovascularization and osteogenesis in the bone site and expedited bone repair.

3D printing is gaining extensive popularity for the pre-modeling of complex biomaterials and for creating patient-specific implants for biomedical applications [65,66]. With the rapidly growing interest, the functionalization of these 3D-printed devices or implants to achieve desired bioactivity in response to the specific application, becomes critical. Surface coating with a layer of materials or biomacromolecules that has the required bioactivity properties, is one of the easiest and most effective solutions to grant bioactivities to the 3D-scaffolds [67]. After coating, the 3D-scaffolds can acquire the desired functions while retaining their original geometrics and mechanics. For bone regeneration, the surface coating may enhance cell adhesion, differentiation, mineralization, as well as osteoconductivity of 3D printed scaffolds, which is essential for new bone formation. As a direct contact between the bone tissue and the implant surface, coatings may also help to inhibit bacterial infection and boost osseointegration after implantation. Depending on the biological requirements of the surrounding tissue, various biomaterials or biomolecules may be applied to 3D-printed scaffolds. These include bioceramics (hydroxyapatite, tricalcium phosphate), nanomaterials (metal–organic frameworks, covalent organic framework), cell-affinity biopolymers (chitosan, collagen), RGD (Arg--Gly-Asp) peptides, anti-infection drugs, and growth factors (BMP-2, VEGF) [67–69].

In this study, we present a promising strategy to enhance the bioactivity of the scaffolds by coating GOBP hetero-nanostructures. The

2D hetero-nanostructure materials are rising stars in the biomedical field [70]. However, the application of 2D hetero-nanostructures in regenerative medicine is rarely explored. Our study provides a pioneering exploration in the field and demonstrates that the specific 2D hetero-nanostructures with cell-affinities, e.g., GOBP hetero-nanostructures, could be utilized for 3D-scaffolds functionalization to enhance *in vitro* stem cell adhesion, proliferation, differentiation, and *in vivo* bone regeneration. After implantation, the coated thin layer of 2D hetero-nanostructures will immediately contact the defect site and release the encapsulated growth factors or immune-regulatory cytokines, to help build a pro-healing environment and facilitate new tissue regeneration [71]. With the ingrowth of tissue, the 3D-printed scaffolds that consist of biodegradable polymers or bioabsorbable ceramics will gradually be degraded and adsorbed *in situ*, making space for complete tissue regrowth [38,71]. The surface coating will either be biodegraded or incorporated into the newly formed tissue, depending on its chemical nature.

Immuno-modulation is an emerging topic for bone regeneration [72,73]. However, limited methods were developed for the facile and effective immuno-function of 3D-scaffolds. Here, we present a promising strategy to enhance the loading of immunoregulative factors to 3D-scaffolds using 2D GOBP hetero-nanostructures. Taking advantage of the large surface area of the 2D materials, these hetero-nanostructures significantly increased the loading content for immuno-regulative IL-4 cytokines to the 3D-printed scaffolds. After implantation *in vivo*, the 3D-scaffold surfaces could release IL-4 cytokines, polarizing macrophages into the pro-regenerative M2 phenotype and promoting osteo-immunomodulation. The combined impact of phosphate release, which fosters cell growth, and IL-4 cytokine's osteo-immune modulation, which generates a microenvironment conducive to regeneration, thereby stimulating neovascularization and osteogenesis in the bone site and accelerating bone healing.

Based on this strategy, future studies may broaden the scope of 2D hetero-nanostructures from GOBP to various types of carbon or phosphorene-based heterostructures. In addition, a large variety of immuno-regulative or immuno-active cytokines or biomolecules, e.g., interleukin 10 (IL-10), type I interferons (IFN-α and IFN-β), and tumor necrosis factor-alpha (TNF-α), may also be applied to the 3D scaffolds by adsorbing onto the 2D hetero-nanostructures. These factors may not only regulate the macrophages, but can be extensively designed for directing other types of immune cells, e.g., T cells and B cells, toward a pro-healing immune environment for bone regeneration [40,74,75].

Taken together, this strategy provides a facile and versatile methodology for the immune-functionalization of 3D-printed scaffolds using 2D hetero-nanostructures. It is a cost-effective method for enhancing the bioactivity of bone tissue scaffolds produced by 3D printing. The 2D hetero-nanostructures may be easily adapted to a large variety of biomaterials, e.g., biodegradable polyesters, bioabsorbable ceramics, inorganic bioglasses, and bioactive natural polymers. With these advantages, the immuno-functionalization of 3D-scaffolds with 2D hetero-nanostructures combined with supplementary immuno-regulative cytokines provides a promising strategy for bone tissue engineering as well as a wide variety of other regenerative medicine applications.

5. Conclusions

In summary, we successfully constructed the immuno-functionalized 3D-scaffolds via combining the 2D hetero-nanostructures and immuno-regulative IL-4 cytokines and optimized *in vivo* bone injury repair by creating a pro-healing immuno-microenvironment. *In vitro* tests showed that the 2D hetero-nanostructure consisting of GO and BP nanosheets could improve cell adhesion with continuous release of phosphate ions to stimulate cell proliferation and osteogenesis. The 2D hetero-nanolayers also increased the loading content for immuno-regulative IL-4 cytokines and modulated the polarization of macrophages into M2 phenotype to build a pro-healing immunological microenvironment for better angiogenesis and osteogenesis. The *in vivo* implantation results showed that the immuno-functionalized 3D-scaffolds bridged the injury defect, enhanced cell recruitment, and stimulated *in vivo* neovascularization and osteogenesis by continuous release of phosphate. The loaded IL-4 cytokine further facilitated the polarization of macrophages into M2 phenotype, which may help in establishing a pro-healing microenvironment for expedited bone injury recovery. Therefore, the immuno-functionalization of 3D-scaffolds with 2D GOBP hetero-nanostructures with secondary loading of immuno-regulative cytokines could provide a promising strategy for 3D-printed scaffolds to support fast bone injury recovery.

Associated content

Supporting Information: SEM of BP nanosheets; SEM of stem cells proliferated on 3D-printed scaffolds; immunofluorescence images of macrophages stained with iNOS/CD68/DAPI or CD206/CD68/DAPI; immunofluorescence images of HUVECs stained with CD31 antibodies.

Ethics approval and consent to participate

All animal work in the present study was proceeded in compliance with the Institutional Animal Care and Use Committee (IACUC) of Mayo Clinic, Rochester, MN.

CRediT authorship contribution statement

Xifeng Liu: Conceptualization, Methodology, Formal analysis, Writing – original draft, revision. **Bipin Gaihre:** Methodology, Formal analysis, revision. **Sungjo Park:** Methodology, Formal analysis, revision. **Linli Li:** Methodology, Formal analysis, revision. **Babak Dashtdar:** Methodology, Formal analysis, revision. **Maria D. Astudillo Potes:** Methodology, Formal analysis, revision. **Andre Terzic:** Methodology, Formal analysis, revision. **Benjamin D. Elder:** Methodology, Formal analysis, revision. **Lichun Lu:** Conceptualization, Methodology, Formal analysis, Writing – original draft, revision.

Declaration of competing interest

The authors declare the following financial interests/personal relationships which may be considered as potential: Dr. Elder is a consultant for DePuy Synthes and SI bone, owns stock options and is on the medical advisory board for Injectsense, and receives institutional support for clinical trials from Stryker and SI Bone. The other authors declare no competing financial interest.

Acknowledgments

This work was supported by the National Institutes of Health grant R01 AR075037 and R01 AR56212. The micro-CT work was supported in part by the Mayo Clinic X-ray Imaging Core.

Appendix A. Supplementary data

Supplementary data to this article can be found online at https://doi.org/10.1016/j.bioactmat.2023.03.021.

References

[1] V. Mironov, T. Boland, T. Trusk, G. Forgacs, R.R. Markwald, Organ printing: computer-aided jet-based 3D tissue engineering, Trends Biotechnol. 21 (4) (2003) 157–161.
[2] S.V. Murphy, A. Atala, 3D bioprinting of tissues and organs, Nat. Biotechnol. 32 (8) (2014) 773.
[3] T. Wallin, J. Pikul, R. Shepherd, 3D printing of soft robotic systems, Nat. Rev. Mater. 3 (6) (2018) 84–100.
[4] M.A. Skylar-Scott, J. Mueller, C.W. Visser, J.A. Lewis, Voxelated soft matter via multimaterial multinozzle 3D printing, Nature 575 (7782) (2019) 330–335.

[5] S. Bose, S. Vahabzadeh, A. Bandyopadhyay, Bone tissue engineering using 3D printing, Mater. Today 16 (12) (2013) 496–504.
[6] T.V. Neumann, M.D. Dickey, Liquid metal direct write and 3D printing: a review, Advanced Materials Technologies 5 (9) (2020), 2000070.
[7] Z. Zhu, D.W.H. Ng, H.S. Park, M.C. McAlpine, 3D-printed multifunctional materials enabled by artificial-intelligence-assisted fabrication technologies, Nat. Rev. Mater. 6 (1) (2021) 27–47.
[8] A.J. Capel, R.P. Rimington, M.P. Lewis, S.D. Christie, 3D printing for chemical, pharmaceutical and biological applications, Nat. Rev. Chem 2 (12) (2018) 422–436.
[9] L.Y. Zhou, J. Fu, Y. He, A review of 3D printing technologies for soft polymer materials, Adv. Funct. Mater. 30 (28) (2020), 2000187.
[10] Y.Y.C. Choong, H.W. Tan, D.C. Patel, W.T.N. Choong, C.-H. Chen, H.Y. Low, M. J. Tan, C.D. Patel, C.K. Chua, The global rise of 3D printing during the COVID-19 pandemic, Nat. Rev. Mater. 5 (9) (2020) 637–639.
[11] G.L. Koons, M. Diba, A.G. Mikos, Materials design for bone-tissue engineering, Nat. Rev. Mater. 5 (8) (2020) 584–603.
[12] C. Ji, M. Qiu, H. Ruan, C. Li, L. Cheng, J. Wang, C. Li, J. Qi, W. Cui, L. Deng, Transcriptome analysis revealed the symbiosis niche of 3D scaffolds to accelerate bone defect healing, Adv. Sci. 9 (8) (2022), 2105194.
[13] L. Zhang, G. Yang, B.N. Johnson, X. Jia, Three-dimensional (3D) printed scaffold and material selection for bone repair, Acta Biomater. 84 (2019) 16–33.
[14] A. Le Duigou, D. Correa, M. Ueda, R. Matsuzaki, M. Castro, A review of 3D and 4D printing of natural fibre biocomposites, Mater. Des. 194 (2020), 108911.
[15] J. Liu, L. Sun, W. Xu, Q. Wang, S. Yu, J. Sun, Current advances and future perspectives of 3D printing natural-derived biopolymers, Carbohydr. Polym. 207 (2019) 297–316.
[16] A.J. Lasprilla, G.A. Martinez, B.H. Lunelli, A.L. Jardini, R. Maciel Filho, Poly-lactic acid synthesis for application in biomedical devices—a review, Biotechnol. Adv. 30 (1) (2012) 321–328.
[17] A.C.R. Grayson, M.J. Cima, R. Langer, Size and temperature effects on poly (lactic-co-glycolic acid) degradation and microreservoir device performance, Biomaterials 26 (14) (2005) 2137–2145.
[18] M.G. Henry, L. Cai, X.F. Liu, L. Zhang, J.Y. Dong, L. Chen, Z.Q. Wang, S.F. Wang, Roles of hydroxyapatite allocation and microgroove dimension in promoting preosteoblastic cell functions on photocured polymer nanocomposites through nuclear distribution and alignment, Langmuir 31 (9) (2015) 2851–2860.
[19] F.K. Kasper, K. Tanahashi, J.P. Fisher, A.G. Mikos, Synthesis of poly (propylene fumarate), Nat. Protoc. 4 (4) (2009) 518–525.
[20] X. Liu, E.T. Camilleri, L. Li, B. Gaihre, A. Rezaei, S. Park, A.L. Miller II, M. Tilton, B. E. Waletzki, A. Terzic, Injectable catalyst-free "click" organic-inorganic nanohybrid (click-ON) cement for minimally invasive in vivo bone repair, Biomaterials 276 (2021), 121014.
[21] K.-W. Lee, S. Wang, B.C. Fox, E.L. Ritman, M.J. Yaszemski, L. Lu, Poly (propylene fumarate) bone tissue engineering scaffold fabrication using stereolithography: effects of resin formulations and laser parameters, Biomacromolecules 8 (4) (2007) 1077–1084.
[22] M. Dadsetan, T. Guda, M.B. Runge, D. Mijares, R.Z. LeGeros, J.P. LeGeros, D. T. Silliman, L. Lu, J.C. Wenke, P.R.B. Baer, Effect of calcium phosphate coating and rhBMP-2 on bone regeneration in rabbit calvaria using poly (propylene fumarate) scaffolds, Acta Biomater. 18 (2015) 9–20.
[23] X. Liu, A.L. Miller, S. Park, M. George, B.E. Waletzki, H. Xu, A. Terzic, L. Lu, Two-dimensional black phosphorus and graphene oxide nanosheets synergistically enhance cell proliferation and osteogenesis on 3D-printed scaffolds, ACS Appl. Mater. Interfaces 11 (26) (2019) 23558–23572.
[24] X. Liu, M.N. George, S. Park, A.L. Miller II, B. Gaihre, L. Li, B.E. Waletzki, A. Terzic, M.J. Yaszemski, L. Lu, 3D-Printed scaffolds with carbon nanotubes for bone tissue engineering: fast and homogeneous one-step functionalization, Acta Biomater. 111 (2020) 129–140.
[25] J. Shao, H. Xie, H. Huang, Z. Li, Z. Sun, Y. Xu, Q. Xiao, X.-F. Yu, Y. Zhao, H. Zhang, H. Wang, P.K. Chu, Biodegradable black phosphorus-based nanospheres for in vivo photothermal cancer therapy, Nat. Commun. 7 (2016), 12967.
[26] X. Liu, B. Gaihre, M.N. George, Y. Li, M. Tilton, M.J. Yaszemski, L. Lu, 2D Phosphorene Nanosheets, Quantum Dots, Nanoribbons: Synthesis and Biomedical Applications, 2021. Biomater Sci-Uk.
[27] A.L. Santos, G. Preta, Lipids in the cell: organisation regulates function, Cell. Mol. Life Sci. 75 (11) (2018) 1909–1927.
[28] W. Wu, X. Shi, C. Xu, Regulation of T cell signalling by membrane lipids, Nat. Rev. Immunol. 16 (11) (2016) 690–701.
[29] Y. Zhang, C. Sun, C. Wang, K.E. Jankovic, Y. Dong, Lipids and lipid derivatives for RNA delivery, Chem. Rev. 121 (20) (2021) 12181–12277.
[30] B. Yang, J. Yin, Y. Chen, S. Pan, H. Yao, Y. Gao, J. Shi, 2D-Black-Phosphorus-Reinforced 3D-printed scaffolds: a stepwise countermeasure for osteosarcoma, Adv. Mater. 30 (10) (2018), 1705611.
[31] X. Wang, J. Shao, M.A. El Raouf, H. Xie, H. Huang, H. Wang, P.K. Chu, X.-F. Yu, Y. Yang, A.M. AbdEl-Aal, Near-infrared light-triggered drug delivery system based on black phosphorus for in vivo bone regeneration, Biomaterials 179 (2018) 164–174.
[32] W.C. Lee, C.H.Y. Lim, H. Shi, L.A. Tang, Y. Wang, C.T. Lim, K.P. Loh, Origin of enhanced stem cell growth and differentiation on graphene and graphene oxide, ACS Nano 5 (9) (2011) 7334–7341.
[33] O.N. Ruiz, K.S. Fernando, B. Wang, N.A. Brown, P.G. Luo, N.D. McNamara, M. Vangsness, Y.-P. Sun, C.E. Bunker, Graphene oxide: a nonspecific enhancer of cellular growth, ACS Nano 5 (10) (2011) 8100–8107.
[34] X. Liu, L. Li, B. Gaihre, S. Park, Y. Li, A. Terzic, B.D. Elder, L. Lu, Scaffold-free spheroids with two-dimensional heteronano-layers (2DHNL) enabling stem cell and osteogenic factor codelivery for bone repair, ACS Nano 16 (2) (2022) 2741–2755.
[35] D. Depan, B. Girase, J. Shah, R. Misra, Structure–process–property relationship of the polar graphene oxide-mediated cellular response and stimulated growth of osteoblasts on hybrid chitosan network structure nanocomposite scaffolds, Acta Biomater. 7 (9) (2011) 3432–3445.
[36] Y. Luo, H. Shen, Y. Fang, Y. Cao, J. Huang, M. Zhang, J. Dai, X. Shi, Z. Zhang, Enhanced proliferation and osteogenic differentiation of mesenchymal stem cells on graphene oxide-incorporated electrospun poly (lactic-co-glycolic acid) nanofibrous mats, ACS Appl. Mater. Interfaces 7 (11) (2015) 6331–6339.
[37] Y. Niu, Z. Wang, Y. Shi, L. Dong, C. Wang, Modulating macrophage activities to promote endogenous bone regeneration: biological mechanisms and engineering approaches, Bioact. Mater. 6 (1) (2021) 244–261.
[38] C. Li, C. Guo, V. Fitzpatrick, A. Ibrahim, M.J. Zwierstra, P. Hanna, A. Lechtig, A. Nazarian, S.J. Lin, D.L. Kaplan, Design of biodegradable, implantable devices towards clinical translation, Nat. Rev. Mater. 5 (1) (2020) 61–81.
[39] T. Wang, J. Bai, M. Lu, C. Huang, D. Geng, G. Chen, L. Wang, J. Qi, W. Cui, L. Deng, Engineering immunomodulatory and osteoinductive implant surfaces via mussel adhesion-mediated ion coordination and molecular clicking, Nat. Commun. 13 (1) (2022) 1–17.
[40] M. Tsukasaki, H. Takayanagi, Osteoimmunology: evolving concepts in bone–immune interactions in health and disease, Nat. Rev. Immunol. 19 (10) (2019) 626–642.
[41] S.-S. Jin, D.-Q. He, D. Luo, Y. Wang, M. Yu, B. Guan, Y. Fu, Z.-X. Li, T. Zhang, Y.-H. Zhou, A biomimetic hierarchical nanointerface orchestrates macrophage polarization and mesenchymal stem cell recruitment to promote endogenous bone regeneration, ACS Nano 13 (6) (2019) 6581–6595.
[42] Y. Zhu, H. Liang, X. Liu, J. Wu, C. Yang, T.M. Wong, K.Y. Kwan, K.M. Cheung, S. Wu, K.W. Yeung, Regulation of macrophage polarization through surface topography design to facilitate implant-to-bone osteointegration, Sci. Adv. 7 (14) (2021), eabf6654.
[43] K.M. Hotchkiss, N.M. Clark, R. Olivares-Navarrete, Macrophage response to hydrophilic biomaterials regulates MSC recruitment and T-helper cell populations, Biomaterials 182 (2018) 202–215.
[44] J. Lee, H. Byun, S.K. Madhurakkat Perikamana, S. Lee, H. Shin, Current advances in immunomodulatory biomaterials for bone regeneration, Advanced healthcare materials 8 (4) (2019), 1801106.
[45] Z. Lin, D. Shen, W. Zhou, Y. Zheng, T. Kong, X. Liu, S. Wu, P.K. Chu, Y. Zhao, J. Wu, Regulation of extracellular bioactive cations in bone tissue microenvironment induces favorable osteoimmune conditions to accelerate in situ bone regeneration, Bioact. Mater. 6 (8) (2021) 2315–2330.
[46] Q. Huang, Z. Ouyang, Y. Tan, H. Wu, Y. Liu, Activating macrophages for enhanced osteogenic and bactericidal performance by Cu ion release from micro/nano-topographical coating on a titanium substrate, Acta Biomater. 100 (2019) 415–426.
[47] I. Cockerill, Y. Su, J.H. Lee, D. Berman, M.L. Young, Y. Zheng, D. Zhu, Micro-/nanotopography on bioresorbable zinc dictates cytocompatibility, bone cell differentiation, and macrophage polarization, Nano Lett. 20 (6) (2020) 4594–4602.
[48] D.-W. Zhao, C. Liu, K.-Q. Zuo, P. Su, L.-B. Li, G.-Y. Xiao, L. Cheng, Strontium-zinc phosphate chemical conversion coating improves the osseointegration of titanium implants by regulating macrophage polarization, Chem. Eng. J. 408 (2021), 127362.
[49] L. Gong, J. Li, J. Zhang, Z. Pan, Y. Liu, F. Zhou, Y. Hong, Y. Hu, Y. Gu, H. Ouyang, An interleukin-4-loaded bi-layer 3D printed scaffold promotes osteochondral regeneration, Acta Biomater. 117 (2020) 246–260.
[50] D.C. Marcano, D.V. Kosynkin, J.M. Berlin, A. Sinitskii, Z. Sun, A. Slesarev, L. B. Alemany, W. Lu, J.M. Tour, Improved synthesis of graphene oxide, ACS Nano 4 (8) (2010) 4806–4814.
[51] X. Liu, A.L. Miller, S. Park, B.E. Waletzki, Z. Zhou, A. Terzic, L. Lu, Functionalized carbon nanotube and graphene oxide embedded electrically conductive hydrogel synergistically stimulates nerve cell differentiation, ACS Appl. Mater. Interfaces 9 (17) (2017) 14677–14690.
[52] L. Chen, G. Zhou, Z. Liu, X. Ma, J. Chen, Z. Zhang, X. Ma, F. Li, H.M. Cheng, W. Ren, Scalable clean exfoliation of high-quality few-layer black phosphorus for a flexible lithium ion battery, Adv. Mater. 28 (3) (2016) 510–517.
[53] H. Wang, X. Yang, W. Shao, S. Chen, J. Xie, X. Zhang, J. Wang, Y. Xie, Ultrathin black phosphorus nanosheets for efficient singlet oxygen generation, J. Am. Chem. Soc. 137 (35) (2015) 11376–11382.
[54] S.F. Wang, L.C. Lu, J.A. Gruetzmacher, B.L. Currier, M.J. Yaszemski, Synthesis and characterizations of biodegradable and crosslinkable poly(epsilon-caprolactone fumarate), poly(ethylene glycol fumarate), and their amphiphilic copolymer, Biomaterials 27 (6) (2006) 832–841.
[55] S. Park, A. Terzic, Quaternary structure of KATP channel SUR2A nucleotide binding domains resolved by synchrotron radiation X-ray scattering, J. Struct. Biol. 169 (2) (2010) 243–251.
[56] S.C. Dhanabalan, J.S. Ponraj, Z. Guo, S. Li, Q. Bao, H. Zhang, Emerging trends in phosphorene fabrication towards next generation devices, Adv. Sci. 4 (6) (2017), 1600305.
[57] R. Gusmao, Z. Sofer, M. Pumera, Black phosphorus rediscovered: from bulk material to monolayers, Angew. Chem. Int. Ed. 56 (28) (2017) 8052–8072.
[58] K. Xiong, Q. Fan, T. Wu, H. Shi, L. Chen, M. Yan, Enhanced bovine serum albumin absorption on the N-hydroxysuccinimide activated graphene oxide and its corresponding cell affinity, Mater. Sci. Eng. C 81 (2017) 386–392.
[59] S.H. Ku, C.B. Park, Myoblast differentiation on graphene oxide, Biomaterials 34 (8) (2013) 2017–2023.

[60] X. Shi, H. Chang, S. Chen, C. Lai, A. Khademhosseini, H. Wu, Regulating cellular behavior on few-layer reduced graphene oxide films with well-controlled reduction states, Adv. Funct. Mater. 22 (4) (2012) 751–759.
[61] H. Li, K. Fierens, Z. Zhang, N. Vanparijs, M.J. Schuijs, K. Van Steendam, N.l. Feiner Gracia, R. De Rycke, T. De Beer, A. De Beuckelaer, Spontaneous protein adsorption on graphene oxide nanosheets allowing efficient intracellular vaccine protein delivery, ACS Appl. Mater. Interfaces 8 (2) (2016) 1147–1155.
[62] J.-M. Kim, Y.-S. Yang, K.H. Park, X. Ge, R. Xu, N. Li, M. Song, H. Chun, S. Bok, J. F. Charles, A RUNX2 stabilization pathway mediates physiologic and pathologic bone formation, Nat. Commun. 11 (1) (2020) 1–17.
[63] X. Qin, Q. Jiang, H. Komori, C. Sakane, R. Fukuyama, Y. Matsuo, K. Ito, T. Miyazaki, T. Komori, Runt-related transcription factor-2 (Runx2) is required for bone matrix protein gene expression in committed osteoblasts in mice, J. Bone Miner. Res. 36 (10) (2021) 2081–2095.
[64] Y. Liu, Z. Yang, L. Wang, L. Sun, B.Y. Kim, W. Jiang, Y. Yuan, C. Liu, Spatiotemporal immunomodulation using biomimetic scaffold promotes endochondral ossification-mediated bone healing, Adv. Sci. 8 (11) (2021), 2100143.
[65] C. Yu, J. Schimelman, P. Wang, K.L. Miller, X. Ma, S. You, J. Guan, B. Sun, W. Zhu, S. Chen, Photopolymerizable biomaterials and light-based 3D printing strategies for biomedical applications, Chem. Rev. 120 (19) (2020) 10695–10743.
[66] S. Beg, W.H. Almalki, A. Malik, M. Farhan, M. Aatif, Z. Rahman, N.K. Alruwaili, M. Alrobaian, M. Tarique, M. Rahman, 3D printing for drug delivery and biomedical applications, Drug Discov. Today 25 (9) (2020) 1668–1681.
[67] N.R. Richbourg, N.A. Peppas, V.I. Sikavitsas, Tuning the biomimetic behavior of scaffolds for regenerative medicine through surface modifications, Journal of tissue engineering and regenerative medicine 13 (8) (2019) 1275–1293.
[68] Y. Jiang, X. Pan, M. Yao, L. Han, X. Zhang, Z. Jia, J. Weng, W. Chen, L. Fang, X. Wang, Bioinspired adhesive and tumor microenvironment responsive nanoMOFs assembled 3D-printed scaffold for anti-tumor therapy and bone regeneration, Nano Today 39 (2021), 101182.
[69] B. Gaihre, M.A. Potes, V. Serdiuk, M. Tilton, X. Liu, L. Lu, Two-dimensional nanomaterials-added dynamism in 3D printing and bioprinting of biomedical platforms: unique opportunities and challenges, Biomaterials 284 (2022), 121507.
[70] S. Zhu, Y. Liu, Z. Gu, Y. Zhao, Research trends in biomedical applications of two-dimensional nanomaterials over the last decade–a bibliometric analysis, Adv. Drug Deliv. Rev. (2022), 114420.
[71] H.F. Pereira, I.F. Cengiz, F.S. Silva, R.L. Reis, J.M. Oliveira, Scaffolds and coatings for bone regeneration, J. Mater. Sci. Mater. Med. 31 (2020) 1–16.
[72] Y. Xie, C. Hu, Y. Feng, D. Li, T. Ai, Y. Huang, X. Chen, L. Huang, J. Tan, Osteoimmunomodulatory effects of biomaterial modification strategies on macrophage polarization and bone regeneration, Regenerative biomaterials 7 (3) (2020) 233–245.
[73] Q. Wang, Y. Feng, M. He, W. Zhao, L. Qiu, C. Zhao, A hierarchical janus nanofibrous membrane combining direct osteogenesis and osteoimmunomodulatory functions for advanced bone regeneration, Adv. Funct. Mater. 31 (8) (2021), 2008906.
[74] F. Yu, R. Lian, L. Liu, T. Liu, C. Bi, K. Hong, S. Zhang, J. Ren, H. Wang, N. Ouyang, Biomimetic hydroxyapatite nanorods promote bone regeneration via accelerating osteogenesis of BMSCs through T cell-derived IL-22, ACS Nano 16 (1) (2022) 755–770.
[75] B. Wildemann, A. Ignatius, F. Leung, L.A. Taitsman, R.M. Smith, R. Pesantez, M. J. Stoddart, R.G. Richards, J.B. Jupiter, Non-union bone fractures, Nat. Rev. Dis. Prim. 7 (1) (2021) 1–21.